Experiment on Nuclear Ordering and Superconductivity in Lithium

K. I. Juntunen and J. T. Tuoriniemi

Low Temperature Laboratory, Helsinki University of Technology,
P.O. Box 2200, FIN-02015 HUT, Finland

REPORT TKK-KYL-012

October 2004

ISBN 951-22-7368-3
ISSN 1455-0806

Abstract

We have investigated the nuclear spin system of lithium at ultralow temperatures. Evidence for a magnetic ordering of the nuclei was found: we observed irreversible behavior at low magnetic fields and high polarizations. The NMR spectra also showed a distinguished low frequency anomaly at the same region. We propose a phase diagram with complex features, and the critical spin temperature was estimated to be $\sim$ 350 nK at zero field. We also cooled the lattice of lithium metal down to $\sim$ 100 μK in attempt to detect the Meissner effect, but efforts to observe superconductivity were not successful.

1 INTRODUCTION

This paper describes our experiments on lithium metal at ultralow temperatures. Our goal was twofold: to examine the low temperature states of both the electronic system and the nuclear spin system. In general, the ground states of the two systems exist independently of each other, but they may have some mutual influence. So far, such interplay phenomena have been investigated in $AuIn_2$ [1], Al [2], Sn [3], Rh [4], and In [5].

For a long time, lithium has been predicted to become superconducting at reasonable temperatures at ambient pressure [6, 7, 8, 9, 10, 11], and it is considered the most probable of the alkali metals to undergo such a transition. Most predictions indicate a T_c at the milli-Kelvin regime, while others range from a few micro-Kelvins to above one Kelvin. However, the experiments have so far revealed no signs of superconductivity at ambient pressure [12, 13]. Under altered circumstances, however, the behavior may change drastically: strongly compressed lithium becomes superconducting already at quite high temperatures extending up to 15 K [14, 15, 16, 17]. Also, a thin film of lithium, deposited at low temperatures, has shown signs of metastable superconductivity with a T_c from 1.2 to 2.4 K with film thicknesses 10 to 200 nm [18].

The large magnetic moment of the ^{7}Li nuclei makes studies of nuclear magnetic ordering in lithium interesting because of the practical feasibility. The long spin lattice relaxation time of lithium is ideal for such experiments, where one is able to maintain a low lattice temperature for times long enough to get the nuclei polarized. Once polarized, one then has ample time to conduct measurements on the slowly warming nuclei.

In a system of nuclear spins, the temperature and magnetic field are closely related to each other. The system behaves adiabatically on slow changes: the entropy $S(B/T)$ is conserved, whence a change in B forces a change on T as well. If, however, collective phenomena exist in the system, the behavior may be nonadiabatic. The magnetization M of the spin system and its entropy are bound to each other by a one to one relationship at high fields. The magnetization (or polarization $p = M/M_{\mathrm{sat}}$) is then a convenient measure of the system's entropy.

This kind of a spin system can be polarized in a high magnetic field, and subsequently adiabatically demagnetized to zero field [19]. The temperature of the nuclei is then reduced to much below the temperature of the electronic system. The strength of the interactions between these two subsystems determines the time scale of reaching the equilibrium between them. In lithium, these interactions are quite weak, and the equilibration is very slow. In our experiments, reaching this equilibrium could take several days.

The temperature of the spin system can not be measured by using any conventional thermometers, because the spin system is not in thermal equilibrium with the electronic system. Instead, it is done by using the second law of thermodynamics: applying a heat pulse and measuring the change in entropy caused by the pulse. From these measurements, the relations between the temperature and the other thermodynamical quantities can be obtained.

The NMR spectra of such a system can be measured both sweeping the frequency and keeping the field constant, and vice versa. For lithium, these spectra consist of several different components: both lithium isotopes' resonances, and also, within the limits of resolution, possibly the multiple spin flip resonances for both isotopes. The resolution in this experiment was good enough to resolve the double spin resonance of ^{7}Li, and also a trace of the triple spin resonance was observed. The positions and widths of the different NMR peaks can give information on the interactions between the spins in the system.

1.1 Properties of lithium

Natural lithium has two isotopes. The dominating isotope ^{7}Li with spin 3/2 and a magnetic moment of $\mu_7 = 3.26\mu_N$ has abundance $x_7 = 92.5\%$. The abundance of the other isotope ^{6}Li with spin 1 and magnetic moment $\mu_6 = 0.82\mu_N$ is $x_6 = 7.5\%$. The small abundance and much smaller magnetic moment make ^{6}Li unimportant compared to ^{7}Li in nuclear magnetism. The minor isotope can, however, be used as a probe nucleus when analyzing the spin-spin interactions.

At room temperature, the lattice of lithium has a well defined body centered cubic (bcc) arrangement. At 70-80K, the lattice undergoes a martensitic phase transition. The low temperature lattice structure is not regular: it has dominatingly a rhombohedral close packed 9R structure, but also face centered cubic order and short range ordered polytypes coexist [20]. The noncubic nature of the lattice gives rise to quadrupolar interactions, but since the quadrupolar moments of both lithium isotopes are small, these interactions are not important. Anderson [21] has investigated dilute Li-Mg alloys at low temperatures and come to the conclusion that the quadrupolar interactions in pure lithium are small; in such alloys, the addition of Mg atoms produces local nonspherically symmetric electric fields that give rise to interactions with the quadrupolar moments of lithium nuclei.

1.2 Basics of nuclear magnetism

1.2.1 Spin-spin interactions

The relevant interaction mechanisms for nuclear magnets are the dipolar force, the conduction electron mediated indirect exchange interaction, and the direct exchange interaction. In electronic magnetism, the exchange interactions dominate over dipolar interactions. The first group, where nuclear magnetic ordering was observed, were some insulators [22]. In them, the electrons are localized to lattice sites, and the dipolar force is the only possible interaction mechanism. Indirect exchange interaction plays a significant role in the formation of the ordered state in the pure metals [23, 24, 25, 26], but the dipolar interaction is important as well. The present work adds lithium to the group of metals with nuclear magnetic order. Regarding spin-spin interactions, lithium differs from the other metals in this group: the interactions between the lithium nuclei are governed by the dipolar forces, like in insulators. The long spin lattice relaxation time indicates weak interactions between the nuclear spins and the electronic system, whence only minute indirect exchange interaction is expected. A nonvanishing direct exchange interaction might also exist, since the lightness of the lithium nuclei facilitates a large zero point motion. In solid ^{3}He, the direct exchange interaction dictates the magnetic behavior of the nuclei, and induces the antiferromagnetic ordering in the compressed state [27]. There the amplitude of the zero point motion is approximately 1/3 of the interatomic distance, while in lithium it is of the order of 10%.

The model Hamiltonian for the system of nuclear spins in simple metals is composed of the Zeeman term, the Ruderman-Kittel exchange term, and the dipolar term [19]. The quadrupolar interactions are neglected here. The Hamiltonian is written as

$$H = -\hbar\mathbf{B}\cdot\sum_i \gamma_i\mathbf{I}_i - \frac{1}{2}\sum_{i,j} J_{ij}\mathbf{I}_i\cdot\mathbf{I}_j + \frac{1}{2}\sum_{i,j} D_{ij}[\mathbf{I}_i\cdot\mathbf{I}_j - 3(\mathbf{I}_i\cdot\hat{\mathbf{r}}_{ij})(\mathbf{I}_j\cdot\hat{\mathbf{r}}_{ij})], \quad (1)$$

where $D_{ij} = \mu_0\hbar^2\gamma_i\gamma_j/(4\pi r_{ij}^3)$, γ_i is the gyromagnetic ratio of the i'th nucleus, r_{ij} is the distance and $\hat{\mathbf{r}}_{ij}$ is the unit vector between spins i and j, $\mathbf{B}$ is the external field, $\mathbf{I}_i$ is the spin operator of the i'th spin, and J_{ij} is the exchange coupling constant between spins i and j. For the lithium isotopes, $\gamma_6/(2\pi) = 6.266$ Hz/μT and $\gamma_7/(2\pi) = 16.5478$ Hz/μT.

The relative magnitudes of the dipolar and exchange interactions can be compared by defining an exchange parameter,

$$R = \sum_i J_{ij}/(\mu_0\hbar^2\gamma^2\rho), \quad (2)$$

where ρ is the number density of spins. A negative R then describes antiferromagnetic exchange interactions, while a positive R stands for ferromagnetic exchange interactions. For comparison, in copper, silver and rhodium these parameters are $R_{\mathrm{Cu}} = -0.42$, $R_{\mathrm{Ag}} = -2.5$ and $R_{\mathrm{Rh}} = -0.9$ [28, 29, 30].

The room temperature density of lithium is $\rho_{300\mathrm{K}} = 4.63 \cdot 10^{28}$ 1/m^3. The low temperature density, needed for our analyses, is obtained by considering the 9R lattice structure with the lattice constants, $a_{9\mathrm{R}} = 0.310$ nm and $c_{9\mathrm{R}} = 2.274$ nm [31]. These give a number density in the 9R state $\rho_{9\mathrm{R},78\mathrm{K}} = 4.76 \cdot 10^{28}$ 1/m^3. The thermal contraction is negligible in the temperature range below this, and we use the value $\rho_{9\mathrm{R},78\mathrm{K}}$ in our analysis of the low temperature data.

1.2.2 Curie-Weiss law

In the mean field approximation, the Curie-Weiss law relates the susceptibility to temperature as

$$\chi = \frac{C}{T - \theta}, \tag{3}$$

where $C = \mu_0 I(I+1)\hbar^2\gamma^2\rho/(3k_{\mathrm{B}})$ is the Curie constant. For Li, $C = 606$ nK. The Weiss temperature θ describes the interactions in the system and it is

$$\theta = (R + L - D)C, \tag{4}$$

where R is the exchange parameter of Eq. (2), L is the Lorentz factor and D is the demagnetization factor. For a cubic lattice, $L = 1/3$; in the noncubic lattice of lithium, the value of L may differ considerably from the value 1/3.

1.2.3 Local field

The local field B_{Loc} describes the average magnetic field at a lattice site created by its interactions with the rest of the lattice. The local field arises from dipolar and exchange interactions, which sum up quadratically as $B^2_{\mathrm{Loc}} = B^2_{\mathrm{Loc,D}} + B^2_{\mathrm{Loc,R}}$. For 9R lithium, we calculate a dipolar local field $B_{\mathrm{Loc,dip.}} = 240\mu$T, which then is a lower limit for the total local field B_{Loc}.

1.2.4 Spin lattice relaxation

The spin lattice relaxation of the polarization p of nuclei in metals at low temperatures is described by [32]

$$\frac{\mathrm{d}p}{\mathrm{d}t} = \frac{T_z}{2\kappa} p[\coth(\frac{T_z}{2T_s}) - \coth(\frac{T_z}{2T_e})], \tag{5}$$

Table 1: Major impurities in lithium, in ppm

Na	Ca	Fe	Si	Cl	N	K
32	57	<4	20	28	118	31

where $T_z = \gamma\hbar B/k_\mathrm{B}$, κ is the Korringa constant, T_s is the spin temperature, and T_e is the electronic temperature. The Korringa constants for lithium and copper are $\kappa_\mathrm{Li} = 44$ sK [33], $\kappa_\mathrm{Cu} = 1$ sK [19]. In general, this relaxation is not exponential (except for $I = 1/2$), but one can define the momentary relaxation time as

$$\tau_1 T_e = \kappa. \tag{6}$$

This relation is valid at fields much higher than the local field, but at very high fields, it breaks down again. At small fields, the relaxation is faster, and the equation (6) can be used if κ is replaced by $\kappa(B)$,

$$\frac{\kappa(B)}{\kappa_\infty} = \frac{B^2 + B_\mathrm{Loc}^2}{B^2 + \alpha B_\mathrm{Loc}^2}, \tag{7}$$

where α is a constant that ideally varies between 2 - 3 in pure materials [34]. The value of α is very sensitive to magnetic impurities, and even small concentrations can cause a large enhancement of α, i.e. a much quicker relaxation [35, 36].

2 EXPERIMENTAL

We purchased the lithium metal from Alfa Aesar [37]. Table 1. shows the major impurities according to the analysis of the manufacturer. The material had 99.97% purity, with less than 4 ppm of magnetic impurities (iron). We measured a residual resistivity ratio of $RRR = 900 \pm 100$ ($RRR = R_\mathrm{300K}/R_\mathrm{4K}$). Lithium is a reactive material, and the metal had to be capsuled to prevent its deterioration. Our tests indicated, that copper would be suitable for the capsule material, whereas silver and gold easily formed an alloy with lithium and would thus not produce low enough contact resistances between the two materials to allow cooling of the sample [38]. Also, the target of our investigations was pure lithium, not one of its alloys. All lithium handling was done in an argon filled glove box to prevent reactions with air. The oxygen content in the glove box was less than 10 ppm.

We prepared two sets of samples, one thin sample stack for the NMR measurements and one pair of bulk samples for search of superconductivity.

The samples were capsuled inside copper foils; to improve the residual resistivity ratios, all copper foils had undergone a heat treatment at 950°C for approximately 7 hours, at a pressure of 1 μbar air. The samples were prepared by pressing lithium against copper. Since the material went through considerable stress, this method allowed the formation of polycrystalline samples only. Some annealing was obtained by heating the samples, but single crystals were not reached.

The samples were cooled down in a two stage adiabatic nuclear demagnetization cryostat [39], which is capable of achieving a minimum temperature of about 100 μK. The I magnet of 9 T was used to polarize the massive copper nuclear stage. The II magnet, which is capable of reaching fields of 7 T, was used for the polarization of our NMR sample. During the present experiments, we used at most 3 T in the II magnet, which was quite sufficient for polarizing lithium. The temperature of the lattice was measured using a Pt-NMR thermometer, and the temperature scale was calibrated by using a Cobalt nuclear orientation thermometer. All wires were thermally anchored either to the mixing chamber cold plate or to the nuclear stage to prevent heating through them.

3 SEARCH FOR SUPERCONDUCTIVITY

Careful magnetic shielding was required for protecting the superconductivity sample from external magnetic fields, because a low superconducting transition temperature implicates a low critical field. Also, supercooling of the normal state may inhibit the formation of a superconducting state, until a field much lower than the critical field is reached. Experience on rhodium indicates that any superconducting materials close to the sample may cause magnetic flux trapping and consequently suppress superconductivity in the sample [40]. Thus, all our coils were made of copper wires to avoid this kind of problems.

3.1 Sample and Experiment

Magnetic impurities can suppress superconductivity. When processing the samples, we avoided any contact of tools containing magnetic materials with the lithium metal, or the copper foils after their heat treatment. Since molybdenum is known to resist very well corrosion caused by lithium, we used a knife made of molybdenum when cutting the metal.

Fig. 1 shows the construction of the sample for the superconductivity experiment. A piece of lithium was inserted inside a half spheroidal cup

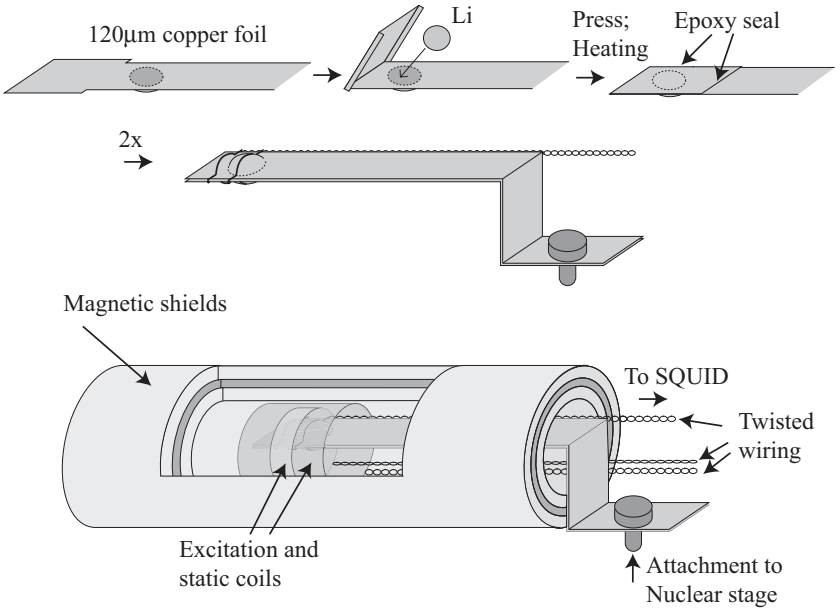

Figure 1: Sample for the superconductivity experiment. The lowest figure (approximately to scale) displays the sample position inside the magnetic shields (cut for illustration) and the coil arrangement.

formed on 120 μm copper foil and a part of the copper foil was bent on top as a lid. The depth of the cup was 1 mm and the radius was 2 mm. The sample was then pressed with a clamp so that the pliant lithium metal filled the cup. The sample in the clamp was heated to 100°C for 10 minutes to ensure good contact between the two metals, and also to obtain some annealing of lithium. The capsule was sealed with a very small amount of Stycast epoxy. Two equal samples were made and they were held together by the pickup loop, which was wound tightly around the samples to ensure a good filling ratio. It was made of 280 μm copper wire. The thick wire had a low resistance, which ensured a low enough high pass frequency of the measuring loop to allow measurements at low frequencies. In addition to the measuring loop, there was also a balancing loop of opposite orientation and equal shape. The two loops were separated by a distance of 0.5 cm.

The samples were inserted inside a magnetic shield and the system was mounted on the nuclear stage of the cryostat. The magnetic shield was made of two concentric high permeability Cryoperm [41] shields with a superconducting layer of lead in between them. This arrangement had a shielding factor of ~ 25000. The magnetic shields are illustrated in Fig. 1.

Sometimes, a superconducting seed material is placed next to the aspired superconductor to take advantage of the proximity effect, but based on the experience gained from the rhodium experiment [40], we had no superconducting materials inside the innermost high permeability magnetic shield. Also, the seed material has to be in direct contact with lithium, and as a corrosive metal, lithium may be contaminated by atoms from the seed material.

The excitation and static fields were aligned with the axis of the magnetic shields, and they were created by two coils inside the shields. The coils were wound on cylindrical copper foils, and the foils were attached to the nuclear stage outside the magnetic shields. The static coil was made of 280 μm copper wire and had 261 turns over 2 cm. The excitation coil was made of 100 μm copper wire, with 84 turns over 0.51 cm. We used excitation levels between 7-70 nT at a measuring frequency of typically 3 Hz.

We cooled the sample down to $(105 \pm 10)\mu$K several times. The trapped static field inside the magnetic shield was estimated to be less than 20 nT. We made an attempt to compensate for the possible remanence fields by sweeping the field slowly between $-1 \ldots + 1\mu$T with the static coil. We estimate, that the field inside the magnetic shields was at best a few nano-Teslas. No superconductivity was observed.

3.2 Susceptibility

In the most recent experiment for ambient-pressure superconductivity in lithium by Lang et al. [13], an unexpected susceptibility signal with a Curie-Weiss temperature dependence was observed. They measured a Curie constant $C = 49\ \mu$K and an antiferromagnetic Weiss temperature $\theta = -2.4$ mK. This signal is not reproduced in our experiments, and the signal could be due to the following reason: in their experiment, lithium was molten on a silver surface. Our tests indicated, however, that lithium and silver form an alloy already at room temperature, but even more eagerly at elevated temperatures [38]. This suggests, that at least part of the sample from Lang et al. may have been Li - Ag alloy [42] instead of pure lithium, and their susceptibility signal might arise from this alloy.

In our experiment, however, we do observe another kind of unexpected susceptibility signal. The susceptibility has a Curie-Weiss behavior with more than an order of magnitude lower C than the signal of Lang et al., and a ferromagnetic Weiss temperature, $\theta \sim 200\ \mu$K.

The signal is definitely not produced by the lithium nuclei, since the magnetic fields ($B < 1\ \mu$T) are much too small to set up any nonzero polarization on them. The time response is also different: the signal changed almost simultaneously with a change in temperature, while at these temperatures, the nuclear spins require hours to reach equilibrium with the lattice when the temperature is changed.

To investigate the origin of the susceptibility signal, we measured an empty copper capsule. It was otherwise prepared exactly the same way as our lithium sample, but with no lithium inside it. From this dummy sample, we observed no susceptibility signal at all. Thus, our signal cannot originate from the copper capsule. Instead, it has to be produced in the electronic system of either lithium, the impurities in lithium, or the interfacial layer between lithium and copper. The work on this phenomenon continues and we are planning to cool down another sample to investigate it further.

3.3 Impurities

Magnetic impurities can suppress superconductivity. In some cases, selective oxidation methods have been used to neutralize these impurities. These methods could not be used in the present case, since lithium itself is susceptible to reactions when exposed to oxygen.

We can compare our situation with impurities to rhodium, which is a superconductor with the lowest currently known transition temperature of all elements, $T_c = 325\ \mu$K [43]. The content of active magnetic impurities in

superconducting samples of rhodium have been 10-20 ppm. The Abrikosov-Gorkov theory predicts a linear decrease of T_c with increasing concentration of magnetic impurities [44], and the estimate for T_c of completely clean Rh is $T_c < 0.5$ mK [43]. Our sample had less than 4 ppm of iron impurities, and a rough scaling in the impurity concentration gives a T_c reduction of at most ~ 0.1 mK. This is a quite rough estimate, since the reduction in T_c depends also on density, impurity spin, exchange interaction between an impurity spin and the surrounding spins, and the density of states at Fermi surface. It can, however, give some kind of an estimate on the magnitude of the reduction.

4 NUCLEAR ORDERING EXPERIMENT

4.1 NMR sample

The NMR sample consisted of 24 thin spots of lithium capsuled inside copper foils of thickness 25 μm. Fig. 2 illustrates the sample, while further details of its preparation have been given in Ref. [45]. Three kind of copper foils of different thicknesses were used to create a suitable thermal path from the sample to the nuclear stage. The changing fields around the sample (ac excitation field and the II magnet field during magnetization and demagnetization) induce eddy currents on the copper foils; they must be as thin as possible to minimize the eddy current heating. A thick foil, on the other hand, gives smaller thermal resistance between the sample and the nuclear stage, and the sample is better cooled. A combination of thin and thick foils was thus used in the thermal path.

The samples were prepared by first diffusion welding the thin 25 μm copper foils ($RRR = 700$) to thicker (115 μm), high conductivity copper foils ($RRR \approx 2000$). Then small lithium pieces were pressed between the thin copper foils with a clamp at a pressure of ~ 100 MPa. Lithium then formed approximately 50 μm thick spots with area ~ 10 mm^2. The samples went through a similar heat treatment as the bulk samples, 10 min at 100°C. Finally, the samples were sealed with a very small drop of Stycast epoxy. The demagnetization factors of our sample were estimated to be $D_y = 0.58$, $D_x = 0.21$ and $D_z = 0.21$ (x-, y-, and z-directions as in Fig. 2).

The copper foils with the lithium samples were spot welded to thicker (1 mm), high conductivity copper foils ($RRR > 2000$), which were attached to the massive copper nuclear demagnetization stage of our cryostat by pressing with screws.

The effectiveness of the thermal path between the nuclear stage and

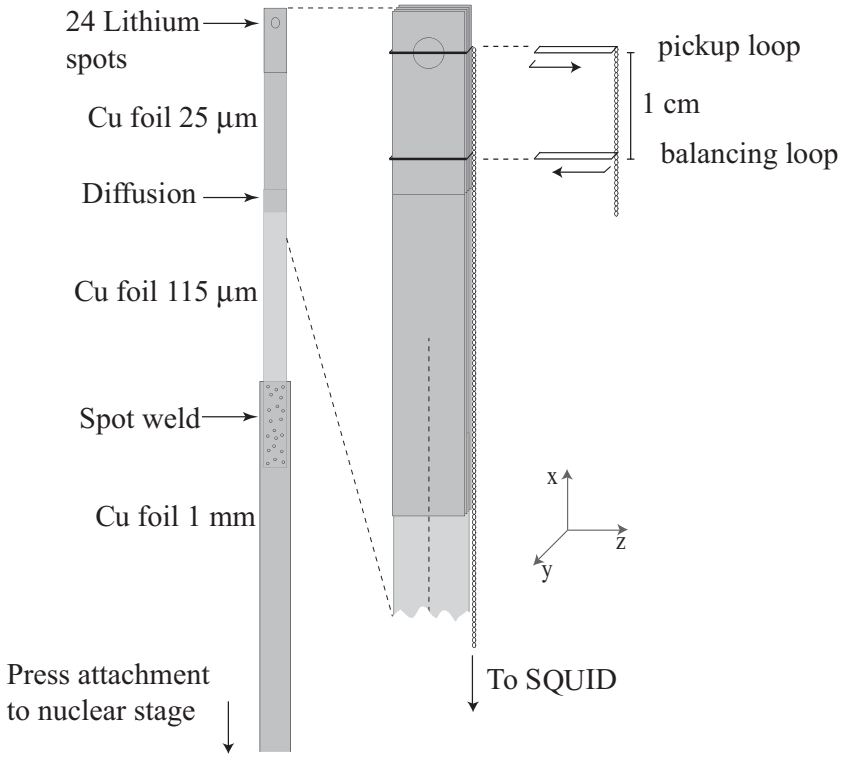

Figure 2: Sample for NMR experiment. The thermal path from lithium to the nuclear stage was made of three different copper foils with thicknesses 25 μm, 115 μm and 1 mm. The pickup loop consisted of a measuring loop and a balancing loop at 1 cm distance.

the samples was evaluated by considering its thermal resistance. To ensure good cooling of the sample, this resistance must be small enough. The heat flow between two objects at temperatures T_1 and T_2 are related by $\dot{Q} = 1/2R_T(T_2^2 - T_1^2)$ [46], where the thermal resistance $R_T = L/(\kappa_0 A)$. Here L is the length and A is the area of the heat path, and κ_0 is the thermal conductivity coefficient. For copper, the Wiedemann-Franz law gives $\kappa_0 = RRR/0.76$ W/(K^{2}m) [46]. The sample is heated by background heat leaks and by the eddy current heating due to ac measurement fields and during demagnetization. We estimate, that these heat leaks are much less than 1 nW. In order to maintain the sample at a low temperature, these heat leaks must be absorbed by the nuclear stage. For the copper foils constituting the heat path between the nuclear stage and the lithium samples, the thermal resistance is calculated to be $R_T = 30$ K^2/W (excluding the thermal resistance of the joints). We made tests to determine the resistance of some spot welded joints, similar to the joints used here, but the resistance was too small to be measured by our equipment (precision was better than 10 nΩ). The diffusion weld between the two copper foils has a thermal conductivity similar to bulk copper. Also, we measured the electrical resistances of several joints between copper and lithium [38], and the corresponding thermal resistances were always much smaller than that of the copper foils forming the heat path. The thermal resistances of the joints can thus be concluded to be negligible.

We estimated, that the heat leaks to the sample will be much smaller than 1 nW; taking the worst case scenario of $\dot{Q} = 1$ nW at a nuclear stage temperature of 300 μK, we get a sample temperature of 380 μK. This allows us to conclude, that the thermal resistance of the heat path is small enough to ensure sufficient cooling of the sample.

We measured the same sample in three different cooldowns, between which the sample was warmed up to room temperature. The bcc lattice structure was then recovered, and again lost in the next cooldown. Because of its ambiguousness, the resulting low temperature structure was probably different than in the previous cooldown. The main NMR results were, however, reproducible between the cooldowns. Thus, the exact lattice structure does not appear to have much influence on the overall behavior of the nuclei. Also, the sample spent some time in air atmosphere between the cooldowns. Had the copper capsulation been deficient, the sample would have deteriorated. The reproducibility of the results evidences, that the sample remained metallic lithium after each warmup.

4.2 Demagnetization cooling

Fig. 3 shows an illustration of the positioning of the sample in the cryostat. The massive copper nuclear demagnetization stage ensured practically constant lattice temperatures during the series of NMR measurements. Several polarization and demagnetization cycles could be repeated before the temperature of the large nuclear stage had risen high enough to require a new precooling. The NMR sample itself acted as the second nuclear demagnetization stage. The sample was first polarized with the II magnet at 1.5 - 2 T at a lattice temperature of 0.3 - 0.55 mK for 10 - 48 hours, and initial polarizations of 60 - 95% of the ^{7}Li nuclei were obtained. The magnetic field was then swept adiabatically, in 40 minutes, to zero. The temperature of the nuclei was thus reduced to much less than the lattice temperature. Because of the large Korringa constant of lithium, the equilibration towards the lattice temperature took several days under the conditions in our experiments, and the measurements described in this paper were performed during this relaxation.

4.3 Squid NMR setup

The pickup coil was made of 280 μm copper wire, and it consisted of a measuring loop and a balancing loop of opposite orientation (see Fig. 2). These loops were at 1 cm distance from each other. The pickup circuit had a resistance of $\sim$ 0.9 mΩ and it was connected to a dc-SQUID (purchased from APS) [47]. The inductance of the SQUID input circuit is 2 μH, and the wiring had an additional inductance of about the same size. The high pass frequency of the system was then around $f_0 = R/(2\pi L) \approx 40$ Hz, which still allowed measurements at 13 Hz, where we measured the quasistatic susceptibility. The linear regime of the SQUID electronics was below 30 kHz, but measurements could well be carried out to over 100 kHz. The pickup circuit was coupled to a compensation circuit, which was used to reduce the background signal level in some of the measurements.

Fig. 4 shows the coils used in the NMR measurements. The x-direction excitation coil had 271 rounds of 280 μm copper wire over a length of 4 cm. Its supporting structure was made of paper, which was hardened with Stycast epoxy. This nonmetallic construction was used to avoid eddy current damping of the excitation. We had another coil of length 3.3 cm made of 100 μm copper wire in the x-direction for creation of static fields. The magnetic fields in the z- and y-directions were created by two saddle coils, which had 80+80 and 40+40 turns and lengths 4.2 and 3.6 cm, respectively. They were made of superconducting 50 μm multifilament wire in a Cu-Ni

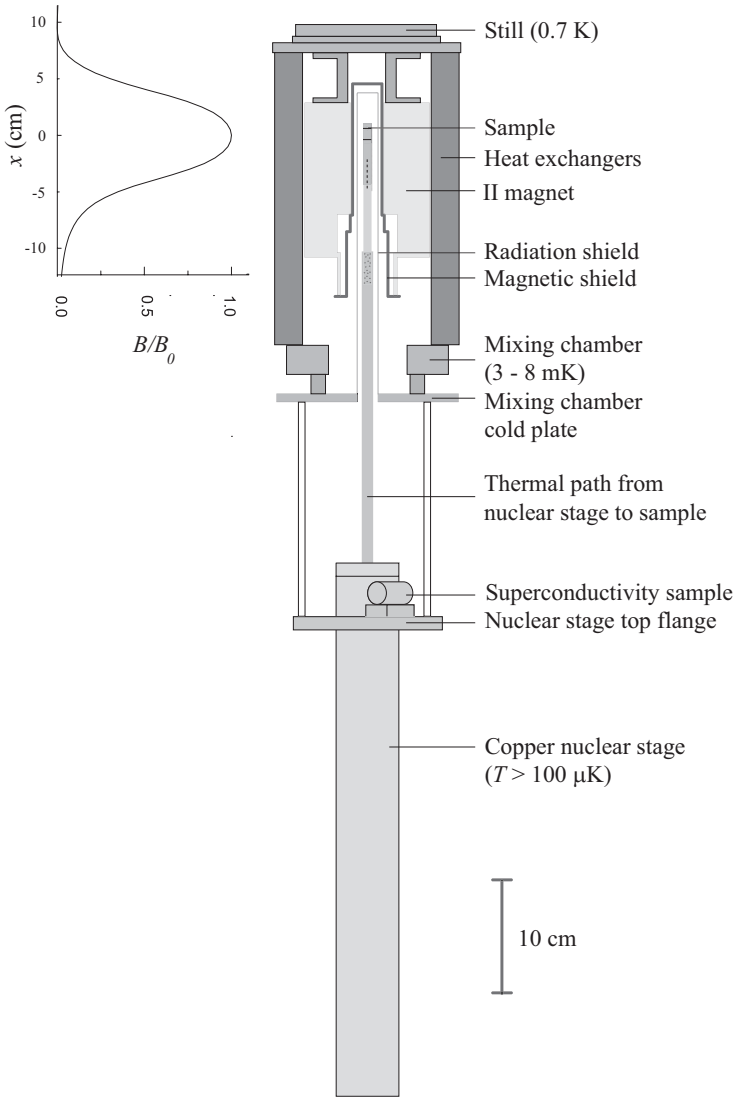

Figure 3: The measurement setup. The coils are not shown in the figure. The sample was attached to the nuclear stage through a thermal path made of high conductivity copper foils. The high permeability magnetic shield (with the saddle coils and the static x-coil mounted to it) was attached to the II magnet, which was mounted to the still (0.7 K). The radiation shield supporting the excitation coil (the coil is not shown in the figure) was attached to the mixing chamber cold plate. The field profile of the II magnet is shown on the left.

matrix. The static x-coil and the saddle coils were attached inside a high permeability magnetic shield, which was mounted to the II magnet (which was anchored to the still). The temperature of this assembly was $\sim$ 1 K, and consequently, a radiation shield was needed to protect the sample from heat radiation from the coils. The radiation shield was made of two insulated layers of 25 μm copper foil and it was attached to the mixing chamber cold plate, whose temperature varied between 3 - 8 mK during the measurements. The excitation coil was inside the radiation shield to prevent eddy current damping, and its structure was supported by the top of the radiation shield.

4.4 Eddy currents

The NMR samples suffer from eddy current effects: at high frequencies both copper and lithium screen the excitation field; the copper capsule also distorts the signal created by the lithium nuclei. The penetration depth describes, how deep the field penetrates a metal at a given frequency, and is defined as $\delta_0 = \sqrt{2/(\sigma\mu\omega)}$, where σ is the electrical conductivity. The thickness of the copper capsule (25 μm) exceeds the penetration depth above 7 kHz. Lithium has smaller conductivity, and the penetration depth does not reach its thickness (50 μm) until 10 kHz. Above these frequencies, we can expect considerable deformations of the signals compared to a situation with no eddy currents. Complicated corrections on amplitude and phase are needed for obtaining the frequency sweep spectra, and the areas of the NMR peaks deviate from an expected behavior. Also, the magnitudes of the ac fields reaching the lithium nuclei differ from the fields created by the coils.

4.5 NMR contribution from copper

In addition to the lithium nuclei, also the copper nuclei of the capsule were polarized when the II magnet was up, and in the polarized state, they generated a signal of their own. The balancing loop in the pickup circuit was designed to reduce the signal from copper to almost zero. Since the balancing was not perfect, some of the copper signal was detected by the SQUID. At small frequencies, the copper signal remained fairly small, but at higher frequencies, the copper signal was enhanced compared to the lithium signal because of eddy current effects. A beneficial fact to our measurements was, that the relaxation of the copper and lithium nuclei are quite different. While the relevant time scale for the relaxation of the lithium nuclei at around T_e = 0.3 mK is some days, the corresponding time for copper is less than an hour.

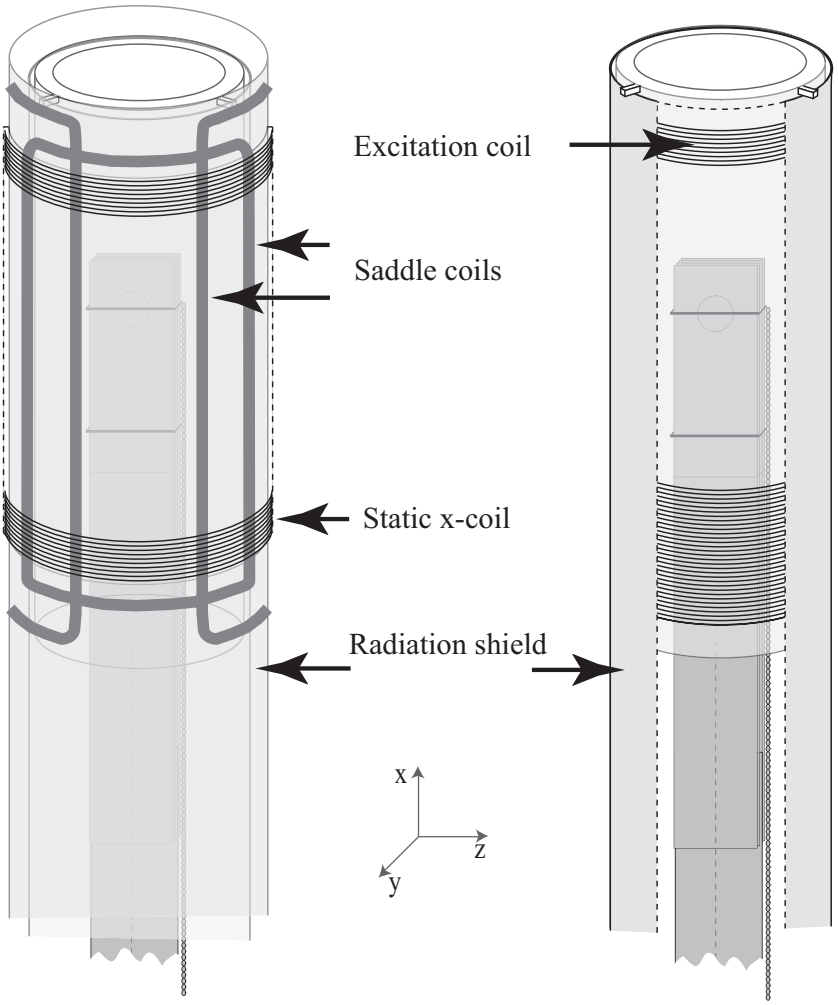

Figure 4: The coils for the NMR measurements. The saddle coils and the static x-coil were wound on a cylindrical copper foil, which was attached to the magnetic shield (not shown in the figure). Inside the cylinder was a radiation shield. The structure of the excitation coil was supported by the top of the radiation shield.

We investigated the effects from copper on our susceptibility signal at 13 Hz. It is possible to obtain a situation, where the copper nuclei are polarized to almost 100%, but the lithium nuclei have only a moderate polarization. Under such circumstances, the decay of the lithium nuclei has a gentle slope, and the possible decay of the signal from the copper nuclei can easily be detected because of the large difference in the relaxation times.

Starting from approximately zero polarization of all nuclei, we polarized the system at 1.5 T, 0.32 mK for 30 minutes, plus the linear magnetization and demagnetization times of 40 minutes. This way we obtained $\sim 95\%$ polarization to the copper nuclei, while the lithium nuclei were polarized to less than 10%. We then measured the susceptibility at 13 Hz. A decay from the copper nuclei was indeed detected: the copper signal had opposite sign than the lithium signal, and it vanished completely in less than half an hour. The magnitude of the decaying signal was, however, very small compared to the maximal signal from lithium, less than 0.5% at largest. Also, the decay of the copper signal was very quick: the zero field relaxation time constant was $\tau_1 = 6$ min. The constant α of Eq. (7) can be calculated for this copper foil: since $\kappa_{\mathrm{Cu}} = 1.2$ sK and $T_e = 0.32$ mK here, we get $\alpha \approx 10$. The copper foil is then not quite clean of magnetic impurities.

A signal from the copper nuclei was also detected in the NMR frequency sweeps; the copper and lithium spectra are separated at high fields, but when the field is low enough, the spectra do overlap. Thus, some of the spectra were seriously disfigured by a signal arising from copper. The same overlap occurs in the NMR field sweeps at low frequencies. However, because of the faster relaxation of the copper nuclei, a wait of about an hour saw to the complete disappearance of the copper signal. The lithium nuclei were then still polarized at best to $\sim 80\%$.

4.6 Calibrations

The absolute value of susceptibility was needed for our analyses, and we resolved it in the following way: We polarized the sample at several different fields for a sufficiently long time to obtain an equilibrium polarization, and often at high temperatures (1 - 7 mK), where the equilibrium state is reached in a reasonable time. The polarization was calculated by solving Eq. (5). We then demagnetized the sample adiabatically to zero, and measured the susceptibility $\chi(13\text{ Hz})$. The relaxation of susceptibility was regular enough to allow extrapolation to the moment when the demagnetization ended, where the polarization could be estimated from known parameters: the polarizing field, the lattice temperature, and the time of polarization. This way we got a calibration for the measured $\chi(13\text{ Hz})$ vs p relation. The absolute value

of the susceptibility was obtained by applying Eq. (8) (the equation will be discussed in the next section) on the susceptibility at high fields.

The calibration between the measured and absolute susceptibility changed due to unknown reasons a few times during the measurements. The new calibration coefficients were obtained by scaling the susceptibilities in such a way, that the original, nonlinear $\chi(13\text{ Hz})$ vs. p relation was reproduced. The scaling factors were at most 1.5.

In the course of the measurements, we were led to suspect that the actual field from the II polarizing magnet was not as expected. This could be due to e.g. the following reason: the sample position was designed to coincide with the maximum in the field profile (Fig. 3); the foil arrangement was, however, bendy, and the actual sample position might have been somewhat shifted up or down from the field maximum. Because of the steepness of the field profile, the actual field could then be lower than expected.

A measurement of the copper nuclei revealed, that this calibration was not right indeed. We polarized the sample using the z direction saddle coil, whose calibration was known, and measured the copper spectra at equilibrium polarization by sweeping the magnetic field at a constant frequency 51 kHz. This frequency is high enough to lift the overlap of the lithium and copper spectra. We then got calibration for the area A versus polarization p relation of copper; the areas of the NMR peaks in the paramagnetic state are proportional to polarization at $B \gg B_{\text{Loc}}$. For copper $B_{\text{Loc}} = 340\mu\text{T}$ [19], and the copper nuclei are definitely paramagnetic at the small polarizations that were used. This $A-p$ relation was used to obtain correct p values of the copper spectra after polarization with the II magnet. From the polarization values, we obtained the calibration for the magnetic field. We found that the magnetic field at the sample was only 70% of the expected value. To summarize the procedure, we first polarized the sample with a known magnet to obtain the calibration for the relationship between p and the NMR-peak area A of the copper nuclei. Then we used this relationship to obtain the polarizations for the nuclei after a polarization with the unknown magnet. When p was known, we could calibrate the magnetic field that created the polarization. The same kind of measurement was not possible for the lithium nuclei, since eddy current effects for lithium were more severe than for copper, and the relationship between the area of the NMR peaks and the polarization is not as simple.

Using the new calibration, we obtained consistent polarization values. The initial polarizations after a demagnetization agreed quite well with the calculated ones. We estimate, that the error in our polarization scale is $< 5\%$.

4.7 Measurement of Polarization

The polarization, magnetic field and susceptibility in the paramagnetic state are related by [19]

$$\chi'(0) = \frac{\mu_0 p M_{\mathrm{sat}}}{B + \mu_0 (D_z - D_x) p M_{\mathrm{sat}}}, \tag{8}$$

where the saturation magnetization for lithium is $M_{\mathrm{sat}} = 0.93$ mT$/\mu_0$ and D_z and D_x are the demagnetization factors along the static and excitation fields, respectively. Our sample is symmetric in these two directions, and D_z and D_x are approximately equal.

Once the scaling factor between the absolute and measured values of the susceptibility has been resolved (section 4.6), this equation can be used for determining the polarization. We measure the susceptibility at 13 Hz. There, the absorptive part of the susceptibility is very small compared to its dispersive part, and we approximate $\chi(13\ \mathrm{Hz}) \approx \chi'(13\ \mathrm{Hz})$. The dispersive part of the susceptibility is also a very flat function of frequency at this frequency scale, and the frequency is small enough to approximate $\chi'(13\ \mathrm{Hz}) \approx \chi'(0\ \mathrm{Hz})$. We then have $\chi(13\ \mathrm{Hz}) \approx \chi'(0\ \mathrm{Hz})$, and we can apply Eq. (8) on this measured quantity. We measure the susceptibility at two fields, 3 mT and 7 mT, much higher than the local field, and use this simple relation for the determination of polarization.

Another method was found more convenient at small polarizations. We found an empirical relationship between the zero field susceptibility and the polarization. This relation was useful at polarizations below $\sim 40\%$, while above that, the susceptibility had different values in different runs (Fig. 11). This is due to irreversible effects, which will be discussed in section 5.8, and is obviously due to ordering.

4.8 Measurement of Temperature

The spin temperature describes the thermodynamical distribution of the spins over the possible energy levels. This quantity has no additional importance, since the polarization (i.e. entropy) gives same information about the system to the experimentalist. However, since the temperature is a more commonly used and understood parameter, we have performed measurements to resolve it.

The spin temperature was determined by using the second law of thermodynamics, $\Delta S = T \Delta Q$. Heat pulses were given to the system by NMR absorption, and the resulting change in entropy was recorded. The energy

absorbed by the spin system per mole is given by

$$\Delta Q = \pi f \chi''(f) B^2 \Delta t V_m / \mu_0, \tag{9}$$

where $\chi''(f)$ is the absorptive part of the susceptibility, B is the amplitude of the external alternating magnetic field at frequency f, Δt is the length of the pulse, and V_m is the molar volume. The entropy S per mole and polarization p of a system of independent 3/2-spins are related through

$$\begin{aligned} S/\mathcal{R} &= u(\coth u - 4\coth 4u) + \ln(\sinh 4u/\sinh u) \\ p &= (4\coth 4u - \coth u)/3, \end{aligned} \tag{10}$$

where $u = \gamma\hbar B/(2k_{\mathrm{B}}T)$, and $\mathcal{R}$ is the molar gas constant. These relations are applicable to a system of ^{7}Li spins at high fields. For ^{6}Li spins, the corresponding relations are different because of the different spin. We ignore here, however, this contribution, since we estimate that the effect would be negligible because of the smaller magnetic moment of the ^{6}Li nuclei and the minor percentage of ^{6}Li. Thus, we treat all spins as 3/2 here and assume a universal temperature over the lithium spins regardless of the isotope.

We measured the nuclear temperature at fields 0 - 2 mT. Fig. 5 shows raw data from one set of experiments. We applied heat pulses on the sample in the measuring field at frequency $f = 1313$ Hz. This frequency was chosen as a compromise between having as low a frequency as possible to avoid eddy current screening, and having a high frequency for bigger absorption at high fields. Between each two pulses, the susceptibility $\chi(B,13\text{ Hz})$ and the high field polarization were recorded. The entropy was then calculated from the polarization by using relations (10), and ΔQ was obtained using Eq. (9). This method set an upper field limit of 2 mT for our measurement, since at very high fields, the absorptive part of the susceptibility, necessary for the determination of ΔQ, was too small to be determined reliably.

The smaller the ΔQ applied on the system is, the more scattered the data is. This is a problem especially at small polarizations. On the other hand, the larger the heat pulses are, the less data we can collect in one run. Because of the latter motive, we used rather small heat pulses and our data at low polarizations are somewhat scattered. At higher polarizations, the scatter is less significant.

The high temperature expansions of the thermodynamical quantities of the nuclear spin system of lithium describe its behavior very well at low nuclear polarizations. We can use a simple second order expansion of the entropy as a consistence check for our temperature measurements. If we assume a universal temperature over all ^{6}Li and ^{7}Li spins, we get the entropy

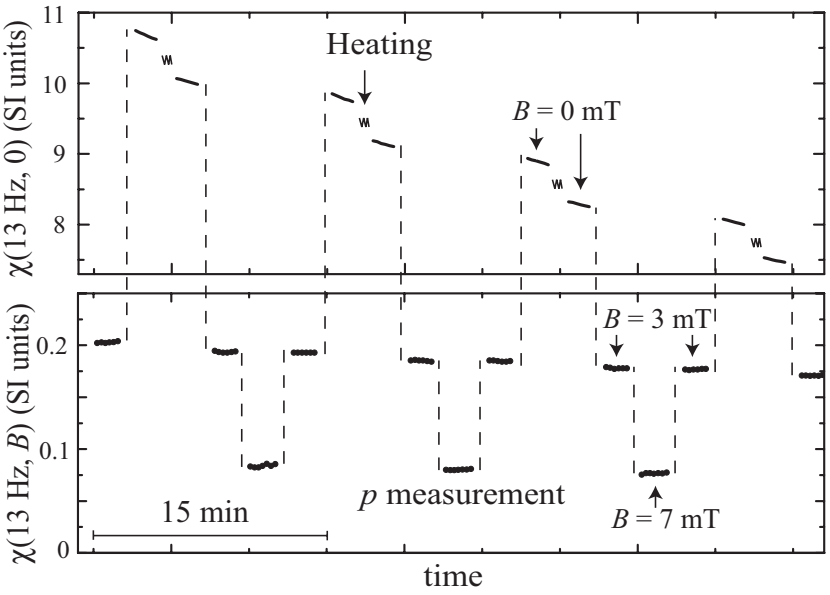

Figure 5: Raw data from heating experiment. The measuring sequence was the following: 1. measure zero field susceptibility, 2. give heat pulse, 3. measure zero field susceptibility, 4. measure polarization (i.e. susceptibility at fields 3 and 7 mT). This sequence was repeated until the system had relaxed to almost zero polarization.

per mole of lithium in second order of $\beta = 1/(k_{\mathrm{B}}T)$

$$S/\mathcal{R} \;=\; a\ln 4 - Ck_{\mathrm{B}}(B^2 + B_{Loc}^2)\beta^2/(2N\mu_0\rho), \tag{11}$$

where $a = x_7 + x_6 \ln 3/\ln 4 = 0.984$. The reduced entropy is $S_{\mathrm{red}} = a - S/(\mathcal{R}\ln 4)$. Fitting the HTE to our data, we obtained an adjustment factor of 2.1, by which amount we had overestimated the heat pulses ΔQ given to the system. The reasons for this are probably eddy current screening of the field, and its possible inhomogeneities. There may also be a small systematic error in determining $\chi''(f)$.

5 RESULTS

5.1 Local field

We obtain a rough estimate for B_{Loc} by fitting the second order high temperature expansions of different fields (described in section 4.8). We get a value $B_{\mathrm{Loc}} = (240 \pm 40)\mu T$, which agrees with the calculated dipolar value, even though the error margin is quite large. Another method of determining the local field is observing the relaxation times at different excitation levels. Using this method, we got quite a high value, $B_{\mathrm{Loc}} = (300 \pm 20)\mu$T. A third method is to examine the longitudinal susceptibility $\chi_\parallel$ as a function of field. In the paramagnetic state, it depends on B and B_{Loc} approximately as [19]

$$\chi_\parallel \propto (1 + B^2/B_{\mathrm{Loc}}^2)^{-3/2}. \tag{12}$$

Usually, this method is used to determine B_{Loc} [19], and functions of the form of Eq. (12) are fitted to the data. Fig. 6 shows some of our $\chi_\parallel$ data at polarizations 0.5 - 40% and fields $-0.12 \ldots 0.12$ mT at frequency 21 Hz. The figure shows considerable narrowing of the susceptibility curves with increasing polarization. We fit functions of the form of Eq. (12) to the data at the very smallest polarizations, where the system has to be paramagnetic. At moderate and high polarizations, we let the exponent n be a free parameter instead of the fixed $-3/2$. This way we get good fits, except at the very highest polarizations, where the peaks are too narrow to be described by a function of this form with any exponent n. The inserts show the B_{Loc} and n obtained from the fits. The solid lines are exponential fits to the data, and there is clear convergence towards the values $B_{\mathrm{Loc}} = (150 \pm 20)\mu$T and $n = -3/2$. This value of B_{Loc} cannot obviously be correct, since the well known dipolar local field is already bigger than this. Some of this discrepancy could be explained with the use of incorrect background values. Also, measuring up

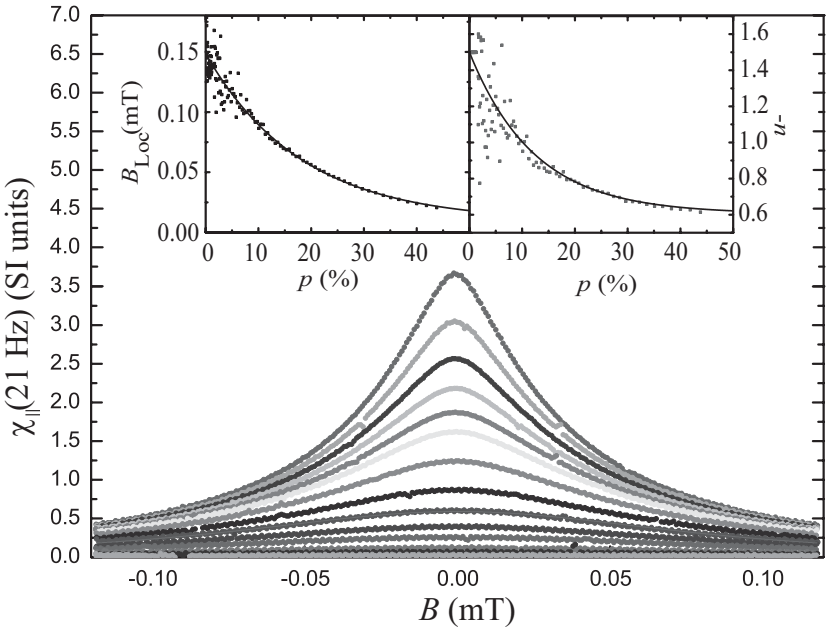

Figure 6: Longitudinal susceptibility $\chi_{\parallel}$ at polarizations 0.5 - 40%. The inserts show the fitting results of the form of Eq. 12 with a free exponent to the data.

to higher fields would have enhanced the accuracy of the fits. These problems can, however, have considerable influence on the results only at the lowest polarizations. The solid lines fit too nicely to the data in the inserts to allow serious doubts about the correctness of the fits, and we conclude that these problems cannot cause the large discrepancy in B_{Loc}. This leads us to the conclusion, that Eq. (12) is not applicable for the case of lithium.

The value of the local field remains then uncertain. Probably, its value is between 240 – 300 μT.

5.2 Spin lattice relaxation time τ_1

We obtained the spin lattice relaxation time by measuring the relaxation of the susceptibility at zero field (and some other fields), and converting the susceptibility into polarization by using the empirical relationship described in section 4.7 Fig. 7 displays the polarization dependence of $1/(\tau_1 T_e) = 1/\kappa$ at fields 0, 0.05 and 4.3 mT. The points come from measurements at several different temperatures between 0.2 - 7 mK. In the figure, a clear hastening of the relaxation is seen with increasing polarization. The solid lines are linear

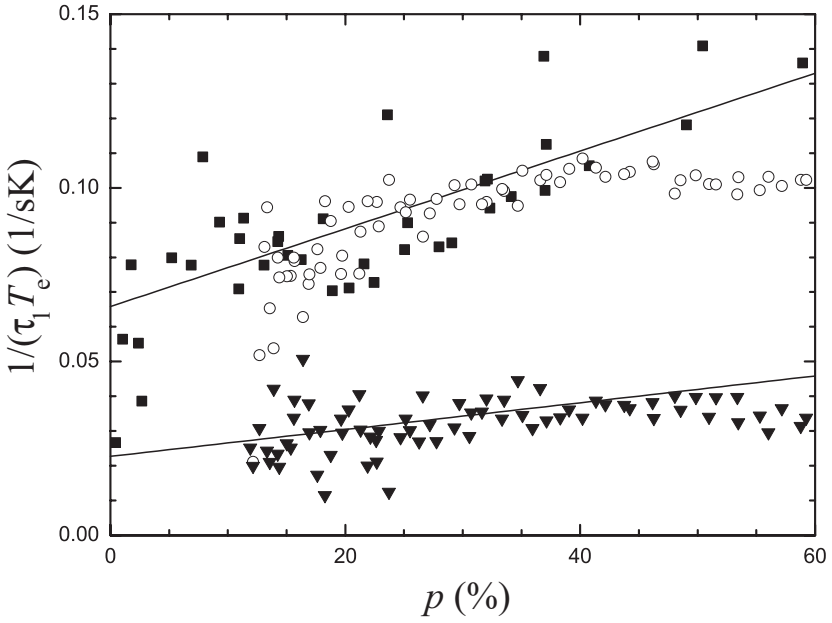

Figure 7: Relaxation rate $1/(\tau_1 T_e)$ of the nuclear polarization at fields 0 mT (solid boxes), 0.05 mT (open circles) and 4.3 mT (solid triangles). Solid lines are linear fits to the low polarization end of the zero field and 4.3 mT data.

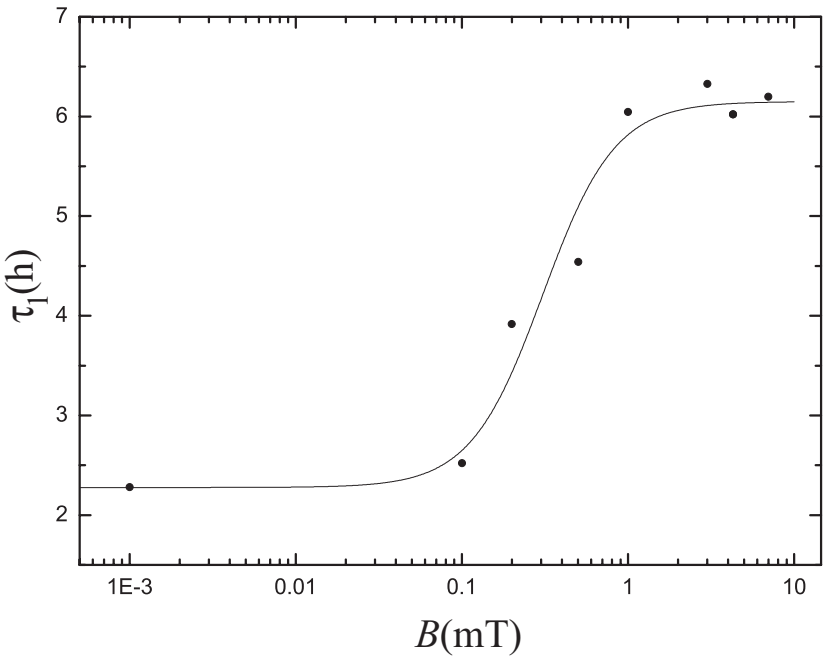

Figure 8: Relaxation time τ_1 as a function of magnetic field at temperature $T_e = 2$ mK. The solid line is a fit of function κ/T_e from Eq. (7).

fits to the low polarization ends of the data. The field 4.3 mT is high enough to agree with the high-field value $1/\kappa = 1/44$ sK at zero polarization. The linear fits give a value for the constant α of Eq. (7), $\alpha = 2.8 \pm 0.2$, which is a fairly typical value for α in a pure material. The data at nonzero fields appear to bend downwards from a linear behavior above $\sim 40\%$ polarization. This is probably due to the onset of irreversible behavior at the same polarization range (section 5.8), but more data would be required to clear the matter. Why the same phenomenon is not seen in the zero field data, remains unresolved.

Fig. 8 shows the relaxation time τ_1 in one of our measurements at 2 mK at several different fields. The points were measured at finite polarizations; an interpolation was made to zero polarization by using an empirical relationship based on such data as shown in Fig. 7. A function κ/T_e (Eq. (7); solid line in Fig. 8) was fitted to the data (with $B_{\rm Loc} = 0.24$ mT). The κ_∞ agrees with the expected value, 44 sK. We also get $\alpha = 2.7$, in agreement with the earlier result.

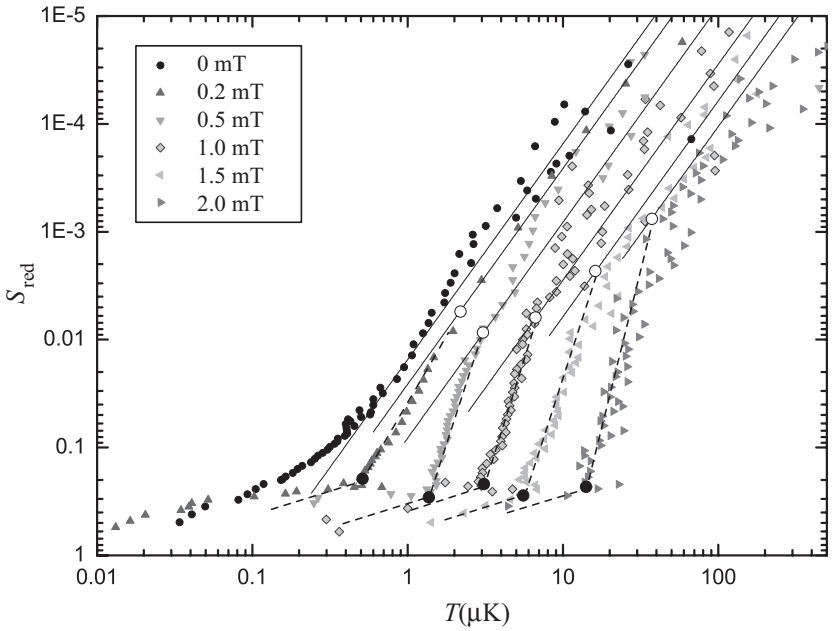

Figure 9: Reduced entropy vs. temperature at fields 0, 0.2, 0.5, 1.0, 1.5, and 2.0 mT. Solid lines are the high temperature expansions of the entropy data at the corresponding fields with $B_{\mathrm{Loc}} = 240\mu\mathrm{T}$. The dashed lines are piecewise linear fits to the data. Open circles denote a deviation from the high temperature expansion, while the solid circles mark a second change of slope of entropy.

5.3 Entropy

The entropy is a measure of disorder in the system. The reduced entropy of the lithium spin system at several fields and their high temperature expansions are shown in Fig. 9 as a function of temperature. The figure shows that the entropy follows its simple second order HTE (which corresponds to the Curie law) well down to a certain temperature. Below that point, the behavior is different in the small field and high field regions. At fields above 0.2 mT, the reduced entropy is clearly higher than the HTE. The points where the HTE breaks down, are indicated by open circles in the figure. At lower temperatures, the entropy drops rapidly (S_{red} increases), until slowing down at a certain point (solid circles). At the zero field data, on the other hand, the reduced entropy is smaller than the HTE at low temperatures.

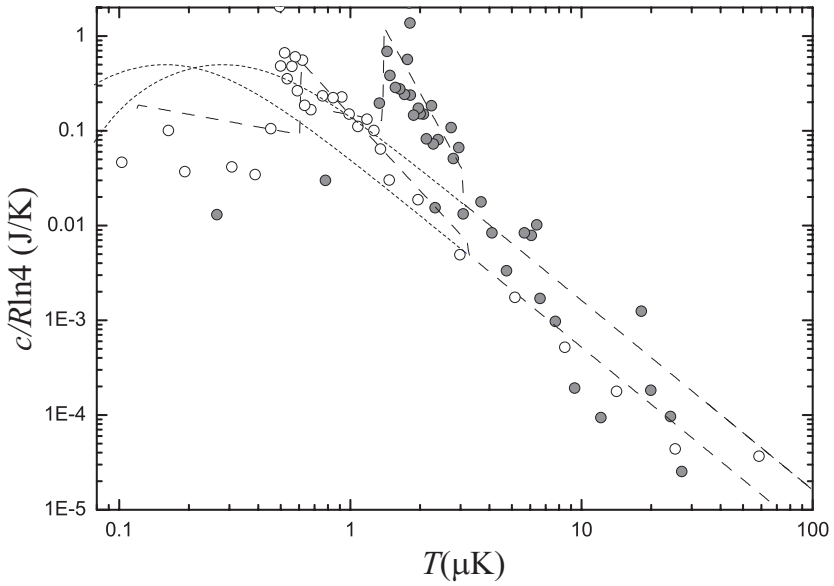

Figure 10: Heat capacity as a function of temperature at fields 0.2 mT (open circles) and 0.5 mT (grey circles). The dashed lines are calculated from the partial linear fits in Fig. 9, and the dotted lines are the heat capacities for free spins.

5.4 Heat capacity

We have not measured the heat capacity directly, but it can be obtained as a derivative from our entropy data,

$$c = \mathrm{d}U/\mathrm{d}T = T\mathrm{d}S/\mathrm{d}T. \tag{13}$$

Taking a derivative from already scattered data gives very irregular data points; Fig. 10 shows the heat capacities at fields 0.2 and 0.5 mT. We plot also the lines corresponding to the partial linear fits of entropy in Fig. 9 at these fields, and the heat capacities of free spins. It is obvious, that the solid circles of Fig. 9 correspond to a maximum in the heat capacity. Proper heat capacity measurements are required to resolve the exact position of these maxima.

5.5 Susceptibility

Figs. 11 and 12 show the quasi static susceptibility χ(13 Hz) as a function of polarization at fields 0, 10, 20, 40, and 60 μT. The paramagnetic behavior is linear (Eq. (8)); at about 5 - 20% polarization, the susceptibilities in the

figures bend upwards from a linear behavior, and above $\sim 70\%$ polarization, the zero field susceptibility saturates to form a plateau approximately at 11 – 12 (SI units). The susceptibilities at small fields show weaker signs of saturation, but no clear plateaus exist. Some zero field data sets show a slight increase in the susceptibility with decreasing polarization at the high-p end.

Above $\sim 40\%$, the value of the zero field susceptibility is not single valued, but forms a band. The susceptibility apparently takes different routes depending the preparation of the initial state and also depending on the conditions of the measurement. In Figs. 11 and 12, the dashed curves limit the possible paths of the zero field susceptibility. All the data shown in the figures come from such measurement sets, where we measured the polarization every now and then, and the polarization of an individual point was obtained through interpolation, i.e. the field was raised to 3 and 7 mT between the zero field measurements. If no visits to non-zero fields had been made, the relaxation of the zero field susceptibility would have been different. As the short uniform chains of data show, the tendency of the susceptibility of the system in an undisturbed state is to decrease monotonously with decreasing polarization. Only a visit to a higher field resulted in the shape seen in Fig. 11. We have, however, no means of obtaining the polarization in the undisturbed state, and cannot present a corresponding figure for such data.

Fig. 13 shows the low polarization end of the susceptibility data. The solid lines are the paramagnetic susceptibilities from Eq. (8), obtained by using $B = \sqrt{B^2 + B_{\mathrm{Loc}}^2}$, and $B_{\mathrm{Loc}} = 240\mu\mathrm{T}$. The figure shows that the susceptibilities at high fields, above 1 mT, do not show significant deviation from the paramagnetic solid lines up to the highest polarizations. At lower fields, on the other hand, the susceptibility follows the relation nicely up to a certain polarization, above which it grows larger than the paramagnetic line. This deviation obviously indicates an onset of some nonparamagnetic state. At zero field, this state appears at less than 10% polarization.

5.6 Weiss temperature θ

The Weiss temperature θ (Eq. (4)) describes roughly the interactions between the spins. Its sign can give interesting information: a negative θ indicates a tendency for antiferromagnetic ordering, while θ is positive in the ferromagnetic case. Usually, this parameter is obtained from the susceptibility data in the paramagnetic state by fitting the Curie-Weiss law with the known C.

Fig. 14 shows the inverse susceptibility of the lithium nuclei at zero field. Unfortunately, our data has too much scatter to obtain reliable values from

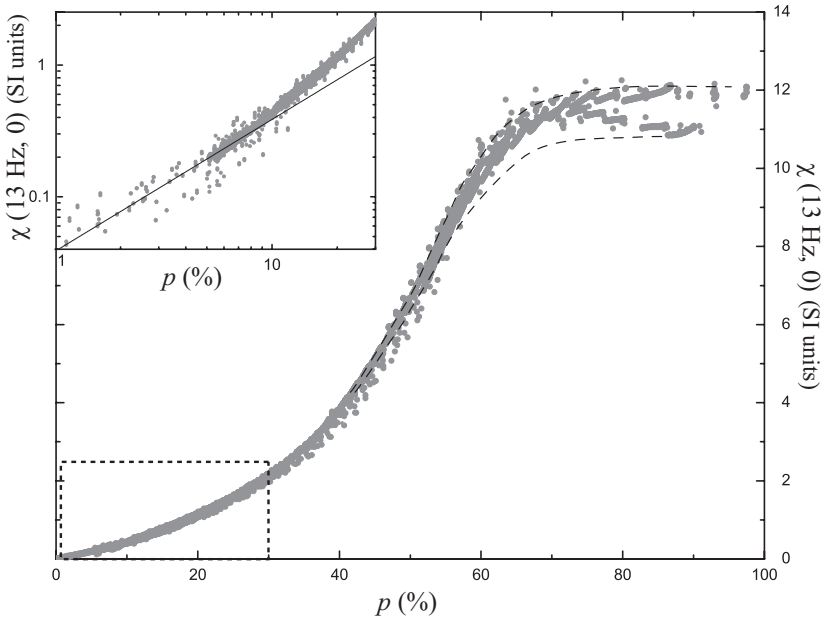

Figure 11: Quasi-static susceptibility (13Hz) vs. polarization at field 0 mT. The dashed lines describe the band, where the susceptibility varies. The insert shows the low-polarization end of the data on a logarithmic axis, and the solid line is the paramagnetic susceptibility from Eq. (8) with $B_{\mathrm{Loc}} = 240\mu\mathrm{T}$.

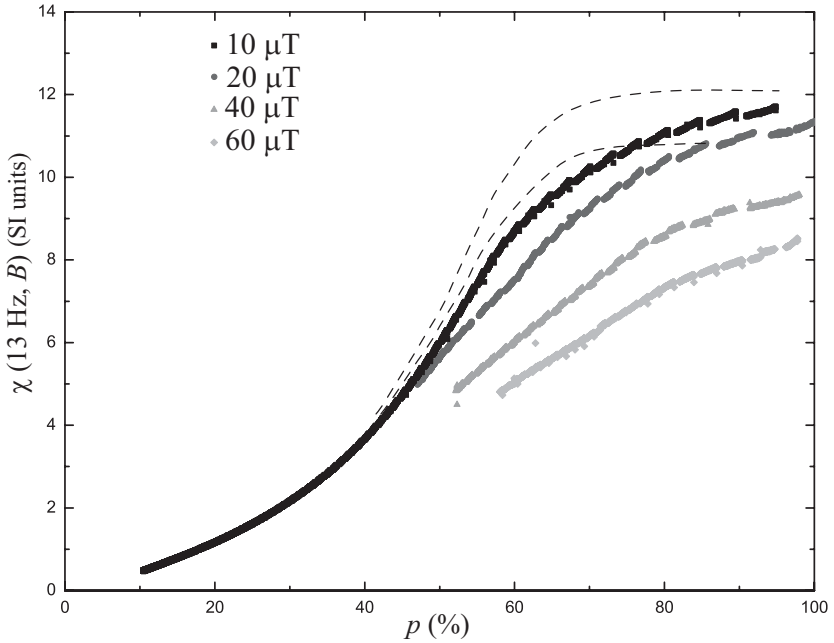

Figure 12: Quasi-static susceptibility (13Hz) vs. polarization at fields 10, 20, 40, and 60 μT. The dashed lines describe the zero field susceptibility band.

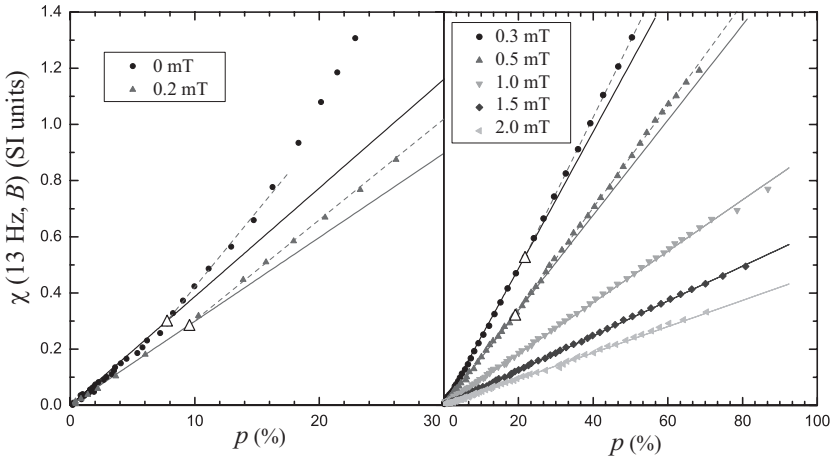

Figure 13: Low polarization end of susceptibility at fields 0, 0.2, 0.3, 0.5, 1.0, 1.5, and 2.0 mT. Solid lines represent the paramagnetic relation (8) at these fields and dashed lines are linear fits to a selected part of the data. The triangles show where the paramagnetic relation breaks down.

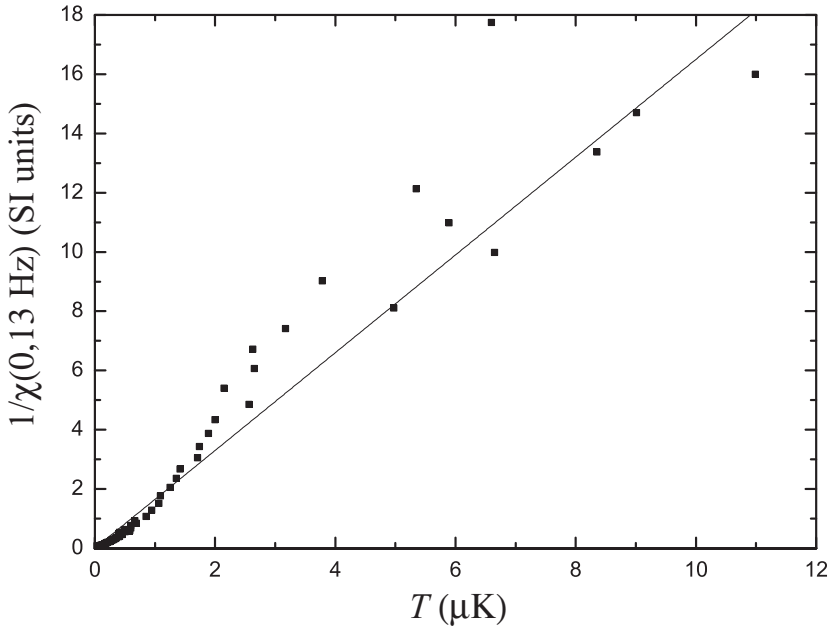

Figure 14: Inverse zero field susceptibility vs. temperature. The solid line is the Curie law with $C = 0.606$ μK.

the Curie-Weiss law fit. The fit gives a small negative value, but since the error margin is larger than the obtained θ, we cannot state that its sign is definitively negative.

5.7 NMR spectra

The NMR spectra can be measured either by choosing a constant magnetic field and sweeping the frequency, or by choosing a constant frequency and sweeping the magnetic field. We did both kinds of measurements, and each have their own advantages and disadvantages. The frequency sweep suffers from complications in background corrections, while for field sweeps the background corrections are trivial, except for overall scaling. The frequency sweeps are also often more noisy, since one can choose to measure the field sweeps at a noiseless frequency. On the other hand, the interpretation of the field sweep data is more problematic: the field is changed under adiabatic conditions, whereby the temperature changes as well with field. No such problems occur with a frequency sweep.

The zero field absorption spectra of Li at very small polarizations have been measured by Anderson already in 1959 [48]. A few years later, he

obtained the spectra at two nonzero fields, 0.8 and 1 mT [21]. Here, we have measured the spectra up to much higher polarizations. Our corresponding low polarization, zero field spectra have approximately the same width, but are located at somewhat (a few kilohertz) lower frequencies. However, our low-p spectra at $\sim$ 300 μT strongly resemble his zero field spectra. Also, his spectra at fields 0.8 and 1 mT agree with our data at about 0.7 and 0.9 mT. His experimental method makes it plausible, that the actual field in his measurements may have been slightly different than thought, which would explain the differences.

Below, we describe the main features of both field and frequency sweep NMR spectra; their further analysis will be presented in Ref. [49].

5.7.1 Background correction in frequency sweeps

Because the lithium was capsuled inside copper, the alternating external field reaching the lithium nuclei was attenuated by eddy currents in copper. Also, the response from the lithium nuclei was attenuated in the copper layer before detection. Because of these effects, a simple background correction using the response at zero polarization was sufficient only at very low frequencies, $f < 100$ Hz. Details of resolving the correct backgrounds have been described in Ref. [45].

5.7.2 Frequency sweeps

We measured the NMR frequency spectra at 16 different fields, (0, 0.02, 0.04, 0.08), (0.12, 0.15, 0.18, 0.25), (0.35, 0.45, 0.6, 0.8), and (1.0, 1.5, 2.0, 2.5) mT at polarizations 0 - 70%. The measurement sets were performed after four different demagnetizations, and in each set, four different field values were measured cyclically. The polarization was measured after each cycle of four field values (grouped as above). The 8 lowest field values were measured on a frequency band of 2 Hz - 30 kHz, the fields 0.35 - 0.8 mT were measured at 30 Hz - 50 kHz, and the highest four fields at 1 - 71 kHz. A logarithmic frequency scale division was used at fields 0 - 0.8 mT; at these fields, we observed interesting effects at low frequencies and needed a dense division there. At higher frequencies, a coarse division was sufficient, and a logarithmic division was then convenient.

Fig. 15 shows the measured spectra at 50 % polarization at frequencies up to 60 kHz at all measured fields. More such spectra have been shown in Refs. [45] and [50]. A special feature of the spectra is that a pronounced peak grows to the low frequency end of the spectrum at low fields and high polarizations. This maximum is interpreted as a sign that there is collective

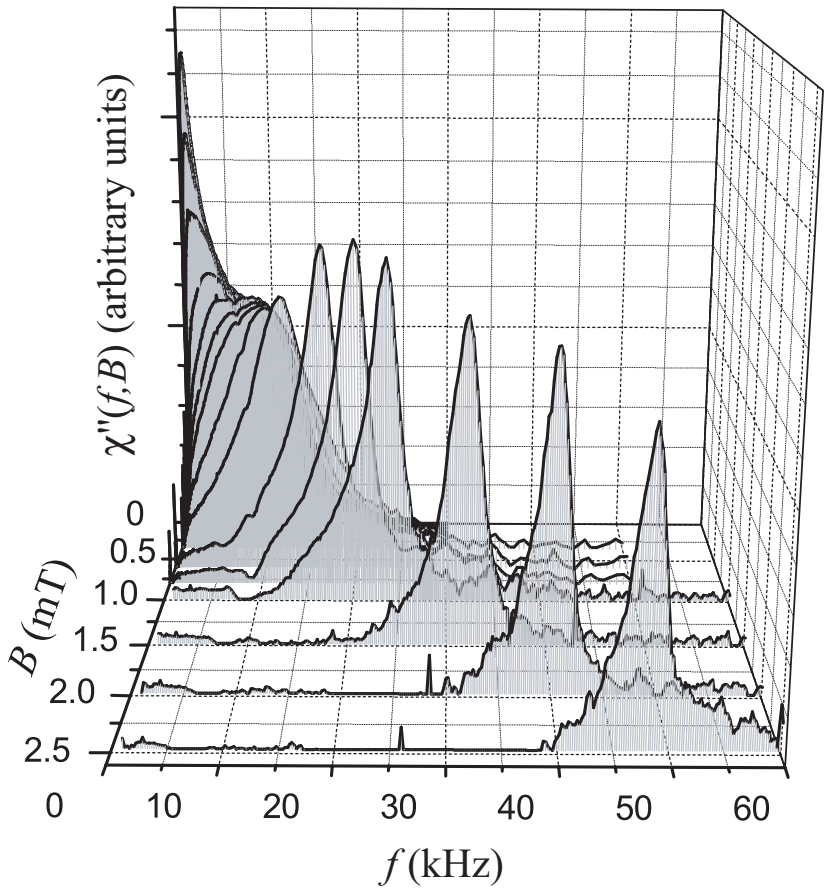

Figure 15: The absorption spectra at 50 % polarization at fields 0 - 2.5 mT and frequencies up to 60 kHz. At low fields, a maximum has grown to the low frequency end of the spectra.

behavior of the nuclei in the system.

To facilitate quantitative analysis of the different peaks, we analyzed the spectra by fitting representative resonance shapes to the data.

The main peaks were asymmetrical, whence a superposition of two similar lines were used to reproduce their lineshapes. At smallest fields (0 - 0.25 mT), best fits were obtained by using a combination of two gaussian lineshapes. To take the new low frequency maximum into account, the spectra at highest polarizations were fitted with two additional peaks having gaussian lineshapes on a logarithmic f-axis. Fig. 16 shows the fits of two such spectra at fields 0 and 0.08 mT at $\sim 50\%$ polarization. The black solid and dashed lines are the gaussian lineshapes with logarithmic f-axes, the grey solid and

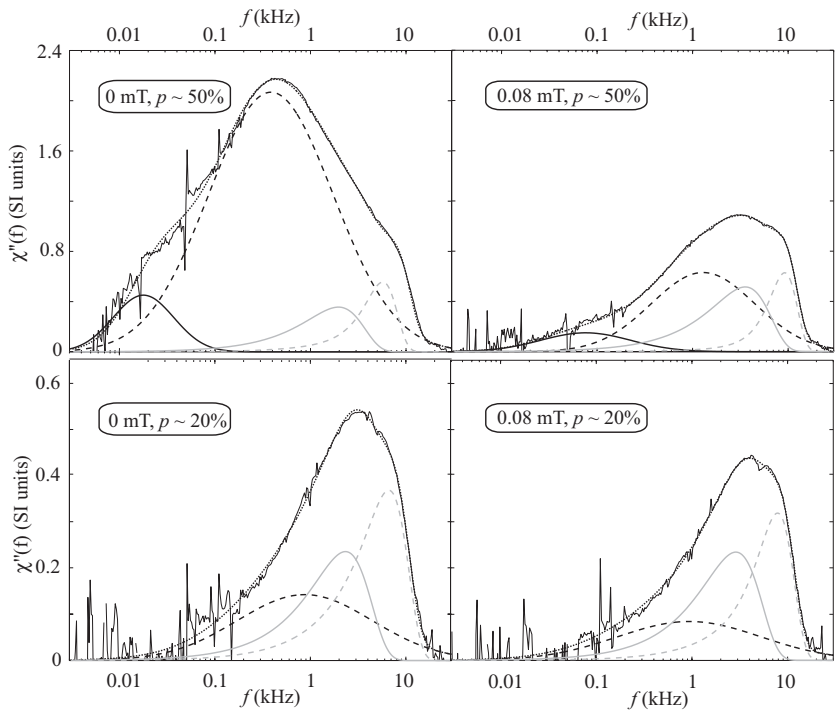

Figure 16: The absorption spectra at 0 and 0.08 mT at $p \sim 20\%$ and $p \sim 50\%$. The black solid and dashed lines are the gaussian fits with a logarithmic f-axis to the low frequency peak, and the grey solid and dashed lines are the gaussian fits of the main ^{7}Li resonance. The dotted line is the total sum of the separate fits.

dashed lines are the gaussian lineshapes with linear f-axes representing the ^{7}Li peak, and the dotted lines are the superpositions of the four lineshapes.

The fields 0.35 and 0.45 mT were fitted using three gaussian lineshapes and one logarithmic gaussian at the low frequency end. The higher fields 0.6 and 0.8 mT were fitted with lineshapes that were lorentzian, but where the peak width was allowed to vary in a gaussian manner, i.e. the width Γ was replaced with $\Gamma \cdot \exp(-(f-f_1)^2/\Gamma_g^2)$, where f_1 is the Lorentzian position of the peak and Γ_g is a "Gaussian width" [51]. This choice of lineshape allowed the peaks to transform from the sharper Lorentzian shapes at high polarizations to the more gaussian like shapes at low polarizations. The best fits for the highest fields 1 - 2.5 mT were obtained with such Lorentzian-Gaussian lineshapes, but one of the lines forming the ^{7}Li single spin flip peak was fitted with a purely gaussian lineshape.

The resulting first moments of the data are shown in Fig. 17. The low frequency anomaly causes the downwards curvature of the data at the smallest fields. The anomalous downshift is emphasized, if the first moments are calculated on a logarithmic frequency axis. A plot of such data is shown in Ref. [50].

The zeroth moments, i.e. areas, of the NMR peaks are shown in Fig. 18. In the paramagnetic state, the areas of the high field peaks should be proportional to the polarization. As the figure shows, the areas grow faster than linearly.

5.7.3 Magnetic field sweeps

We measured the field-sweep NMR spectra at frequencies 5 - 41 kHz. The measurements were conducted after two separate demagnetizations. In the first run, we measured the spectra at frequencies 5111, 7111, 9111, 11111, 16111 and 21111 Hz. We measured these frequencies cyclically, and each sweep was performed back and forth for averaging. The field varied between 0 - 4 mT. We wished to use as high excitation levels as possible to obtain data of good quality, but we also wished to avoid heating the system by excitation. For these reasons, we used an excitation of 85 nT at fields below 1.5 mT, and above that we used a three times higher excitation. The higher excitation could be used, because there we were off the ^{7}Li resonance and the absorption of energy by the spin system was weaker. By increasing the excitation, we were able to obtain better data on the ^{6}Li peak.

In the second run, we measured the frequencies 13111, 18111, 26111, 31111, 36111 and 41111 Hz at fields 0 - 3.5 mT. Here, a constant excitation of 85 nT was used.

Fig. 19 shows the spectra at frequencies 5 - 41 kHz at polarizations 5%,

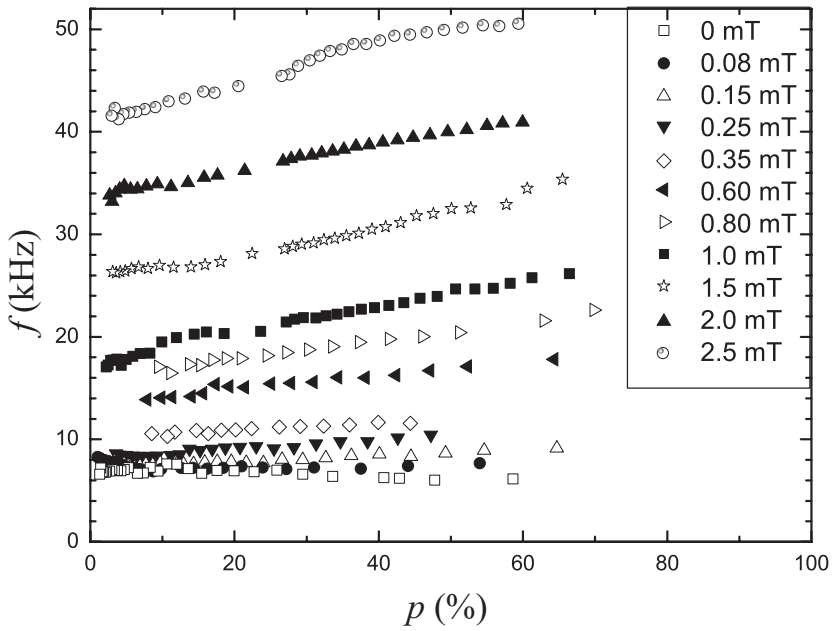

Figure 17: The first moments of the NMR spectra at several fields.

25%, 45% and 65%. Here the spectra are obtained by superposing two consecutive spectra in correct proportions to describe the spectrum at the stated polarization. The ^{7}Li double spin flip peak is clearly visible at the higher-p graphs at approximately half of the main peak position at frequencies 10 - 30 kHz. The resonance of the ^{6}Li nuclei exists, but can only vaguely be resolved in these figures. The amplitude of the peaks is decreasing with increasing frequency, which is mainly a consequence of eddy current damping of the excitation field. The vertical scales of the figures were chosen in order to obtain the same areas in the high frequency peaks in each figure.

Fig. 20 shows the spectra at frequencies 11, 18, 31 and 41 kHz at polarizations 0-70%. In the upper graphs, the ^{6}Li resonance can be seen at high polarizations: at $\sim$ 0.17 mT in the 11 kHz graph, and at $\sim$ 0.28 mT in the 18 kHz graph. The ^{7}Li double spin resonance is clearly visible in all figures. The case for the triple spin resonance was not so clear, since its amplitude will in any case be much smaller than the double resonance's, and it is located on the tail of the double resonance. Fig. 21 shows one spectrum at a polarization of $\sim$ 40%; here we used an excitation amplitude of 0.3 μT at a frequency 21 kHz, and swept the field between 0 and 2.0 mT. One can see some extra intensity on the double resonance's low field tail, centered at about 0.3 mT. This may be due to the triple resonance. To learn more of

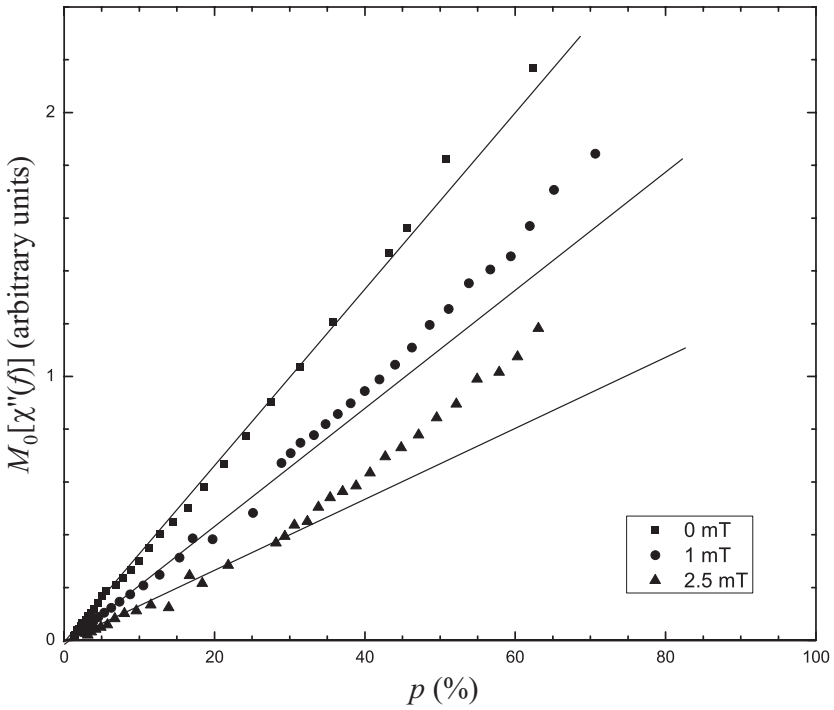

Figure 18: The zeroth moments of the NMR spectra at fields 0, 1.0 and 2.5 mT.

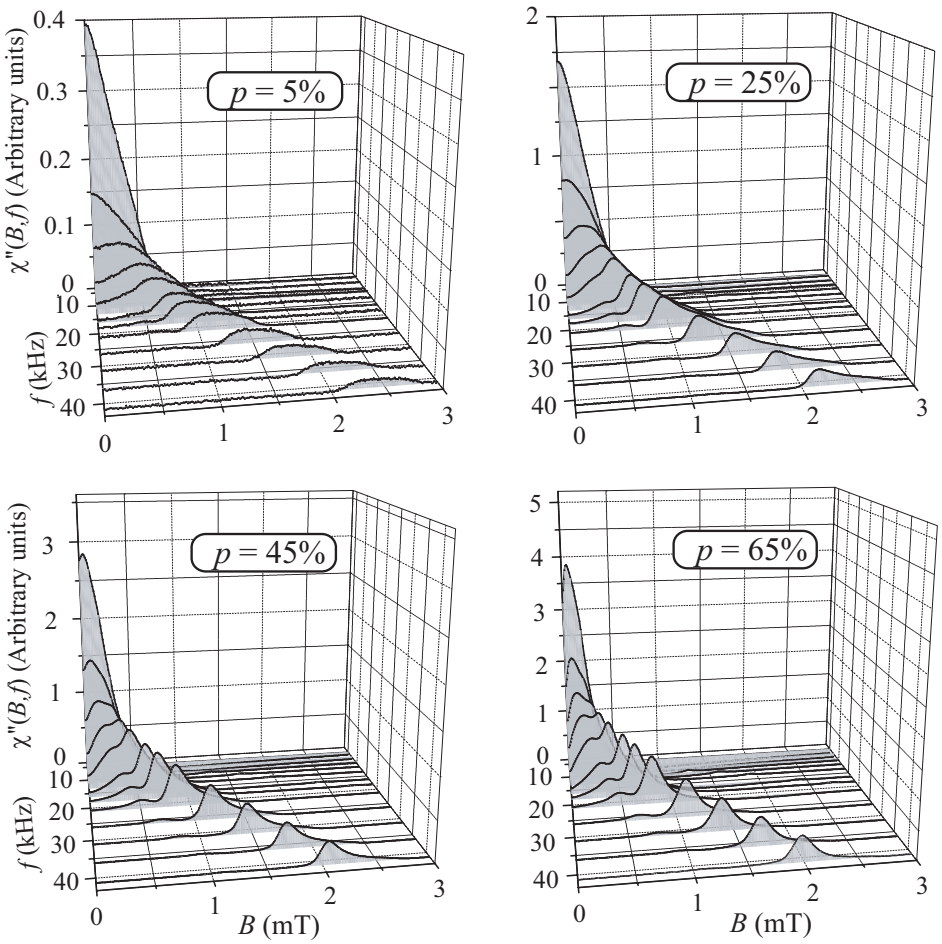

Figure 19: The field sweep spectra at frequencies 5 - 41 kHz at 5%, 25%, 45%, and 65% polarizations. The $\chi''(B)$ is in arbitrary units. The vertical scale is scaled with polarization.

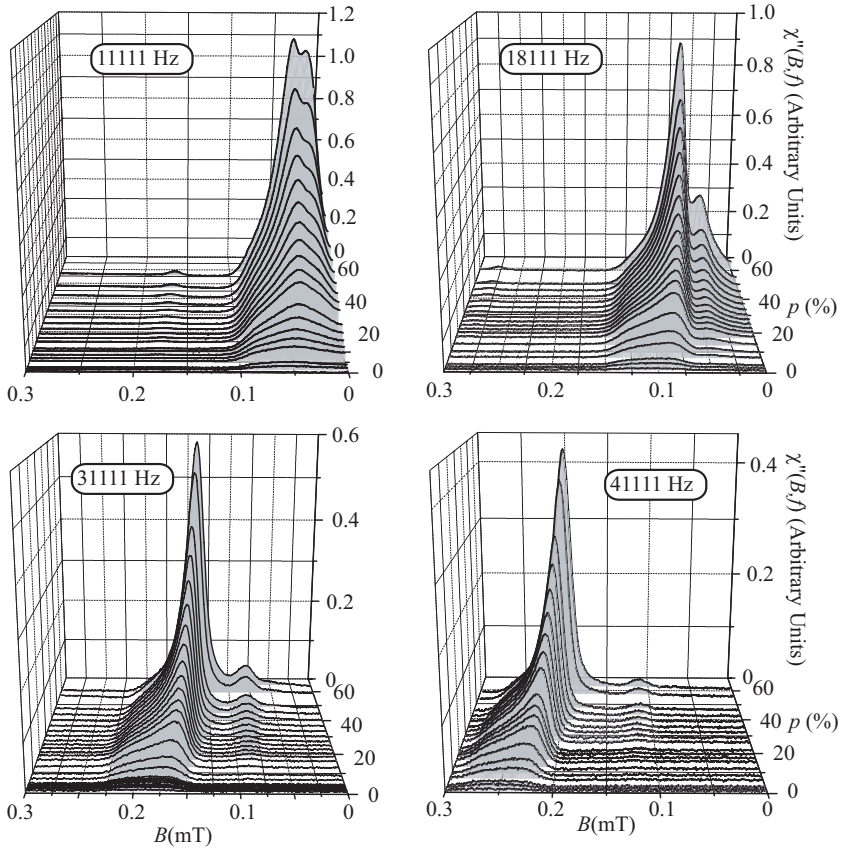

Figure 20: The field sweep spectra at frequencies 11, 18, 31 and 41 kHz at polarizations 0 - 70 %. The scale $\chi''(B)$ is in arbitrary units. The ^{6}Li resonance is seen in the upper graphs. The one and two spin flip peaks of ^{7}Li are visible in all figures.

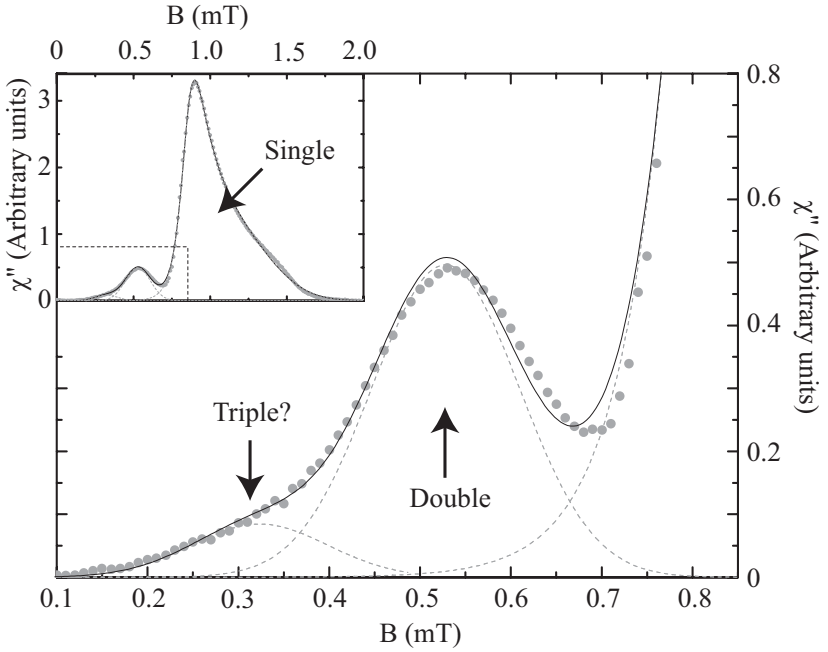

Figure 21: Single spin resonance, double spin resonance and the possible triple spin resonance. The insert shows the whole spectrum, while the main frame shows a magnification of the low fields. Dashed lines are the individual fits to the peaks, and the solid line is their sum.

its nature, we first fit a Lorentzian-Gaussian function to the single spin resonance, and a Gaussian to the double resonance. Keeping these fits constant, we add another gaussian lineshape, located at the low field bump, to the fit. The resulting lineshape with three different peaks is drawn as a solid line in the figure. The dashed lines show the individual peaks. The positions of the peaks are 0.32 mT, 0.53 mT and 1.05 mT, and these relate to each other as 0.31:0.5:1. At zero polarization, the positions of the triple, double, and single spin flip peaks should relate as 1/3:1/2:1. The position of the extra intensity then supports its identification as the triple spin resonance.

5.7.4 Exchange parameter R

The positions of the NMR peaks give information of the interactions in the system. The exchange interaction does not affect the position of the single spin flip peak, while the double spin flip peak is, however, affected. The positions of the resonances can then be used to determine the exchange parameter R. According to theory, the positions of the single spin flip peak

(f_1) and the double spin resonance (f_2) are given by [28, 52]

$$\begin{aligned} f_1 &= f_0 + 3(L-D)\gamma/(2\pi)\mu_0 M_{\mathrm{sat}} p/2 \\ f_2 &= 2f_0 + 2(R+L-D)\gamma/(2\pi)\mu_0 M_{\mathrm{sat}} p, \end{aligned} \tag{14}$$

where $f_0 = \gamma/(2\pi)B$. We do not know the value of $L - D$ exactly, and we combine these two relations to get an equation containing only R,

$$3/2 f_2 - 2f_1 = f_0 + 3R\gamma/(2\pi)\mu_0 M_{\mathrm{sat}} p. \tag{15}$$

Fig. 22 shows the first moments of the single spin flip and double spin flip peaks at a field 1 mT. We fit linear functions of p to these data, as well as on the data at fields 0.45 - 0.8 mT. Using Eq. 15 on the linear coefficients, we get estimates for R. The same analysis can also be performed on the field sweep data at frequencies 26 - 41 kHz. Combining the results from the f- and B-sweeps, we obtain $R = -0.3 \pm 0.15$. It was surprising, though, that we were not able to determine R more accurately than this; there seemed to be a tendency for increasing R with decreasing B in the frequency sweeps, and with decreasing f in the field sweeps. This analysis may then be an oversimplification of the real situation. The sign of R is considered reliable, though, since all fits yield a negative value for it.

The value we obtained is close to the R for copper ($R_{\mathrm{Cu}} = -0.42$). A negative R was not, however, expected for lithium; taking the Ruderman-Kittel formula for indirect exchange interaction parameters [53] (with $k_{\mathrm{F}} = 1.11 \cdot 10^{10}$ 1/m) [54], we get a positive exchange parameter J_1 at the nearest and next nearest neighbor distances. Since the indirect exchange interaction vanishes rapidly with distance, no other than a spin's few nearest neighbors can have considerable exchange interactions with it. R should then certainly be positive.

We must also calculate the factor $L-D$ from the fits, and we get $L-D = 0.35 \pm 0.15$. For a cubic lattice, the Lorentz factor $L = 1/3$. The lithium lattice is not cubic, and obviously its Lorentz factor is much bigger than in the cubic case: with the calculated value (section 4.1) $D \sim 0.2$, we have $L \sim 0.55$. The error margin is, however, quite large.

In addition to giving information of the interactions, the positions of the peaks (at $p = 0$) also allowed a check on the calibration of the current-field relationship of our z direction saddle coil.

5.8 Irreversible effects

A nuclear spin system should behave adiabatically and reversibly on all slow changes of field in the paramagnetic state. Any irreversible behavior is then

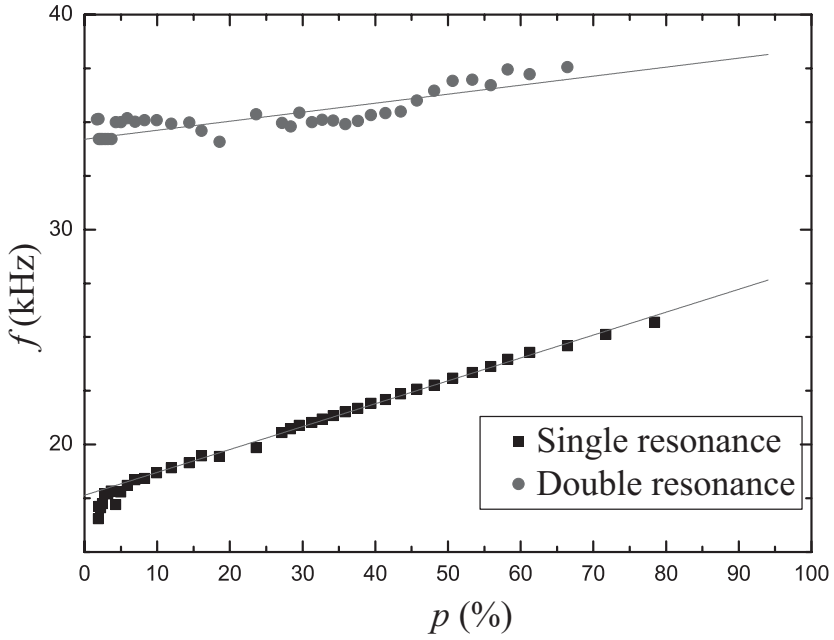

Figure 22: The first moments of the single spin flip and double spin flip ^{7}Li resonances at 1 mT.

a sign of the existence of a nonparamagnetic state. This kind of irreversible behavior was seen in the lithium nuclear spin system at low magnetic fields and high polarizations: when changing the magnetic field, even slightly, and then returning to the original settings, we observed a change in susceptibility. Often, the susceptibility decreased, but in some cases, it even increased. The change in susceptibility was in general the larger the smaller the field, and above 0.25 mT, the effects became too small to be detected by our measurement system. It was also observed, that the irreversible effects exist only above a certain polarization. Fig. 23 shows some data from one run, at polarizations from above 90% to about 60%.

To obtain systematic information on the irreversible effects, we investigated the system at fields 0.01 - 0.25 mT. We applied a transverse, slowly alternating field (0.5 Hz) to the system for a certain time, and then returned to the original field. The magnitude of the disturbing field was chosen to change the direction of B to an angle of 45° with the original field. Before and after the disturbance, we monitored the susceptibility χ(13 Hz) at a constant field of 0.05 mT to quantify the effect of the disturbance. We applied the alternating field for different times (0.2 - 15 min), depending on the strength of the effect, and calculated the change per one period of application

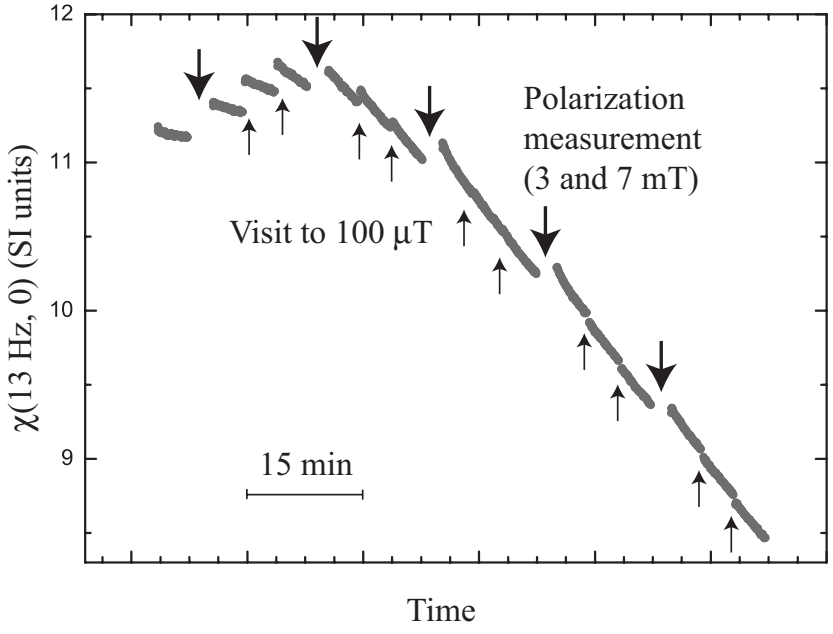

Figure 23: The susceptibility $\chi(0, 13 \text{ Hz})$ from one of the measurements as a function of time. The gaps with thin arrows denote a visit to 100μT, and the gaps with thick arrows denote the measurement of polarization, i.e. a visit to 3 and 7 mT.

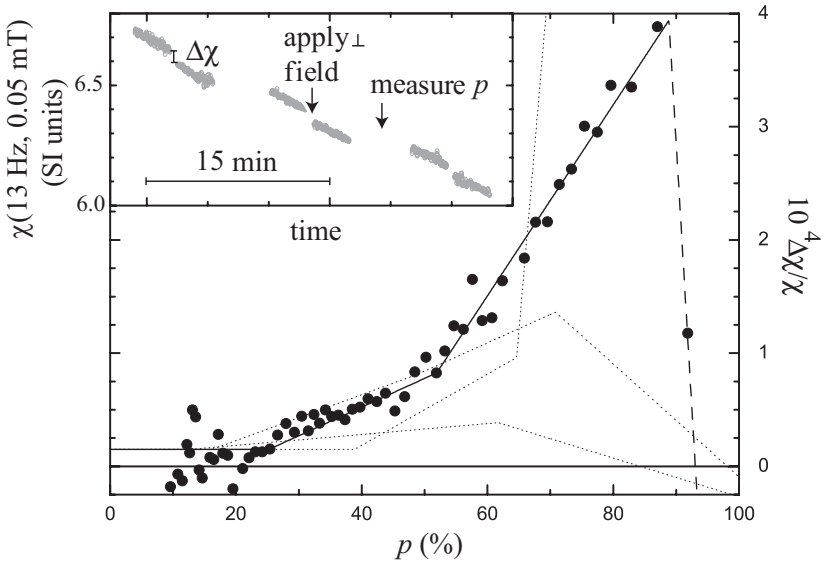

Figure 24: Change in susceptibility χ(13Hz, 0.05 mT) after application of one period of the transverse field in field 0.05 mT. The solid line is a piecewise linear fit the the data with a constant value at low polarizations. The dotted lines are fits to the corresponding data measured at 0.01, 0.1 and 0.25 mT. The insert shows the raw data from the measurement at $p \sim 70\%$.

of the alternating field. This was done by fitting linear functions to the data before and after. This method gives rise to a small offset value in the results.

Fig. 24 shows the data so obtained as a function of polarization in one of the measurements, at field 0.05 mT (incidentally same as the measuring field). The figure sketches also the behavior of the data at fields 0.01, 0.1 and 0.25 mT. Some further data have been shown in Ref. [50].

The data show surprising features: at small polarizations, $\Delta\chi/\chi$ is constant, its offset value. At a certain polarization, the irreversible effects appear, and $\Delta\chi/\chi$ gains a positive slope. At a further point, the low field data ($B < 0.1$ mT) gain an even steeper slope (as the 0.05 mT data in Fig. 24 at $p \sim 50\%$). In addition to these features, the data at high fields (above 0.05 mT) have a maximum point; at polarizations above this point, the data bend downwards (in the 0.05 mT data in Fig. 24, there is only one point representing this behavior; many more such downwards bending points at other fields can be seen in the figures presented in Ref. [50]. The nonadiabatic behavior then disappears at very high polarizations at fields $B \geq 0.05$ mT. The low field data show no such downwards curvature up to the highest polarizations.

In a study of the nuclear spin system of polycrystalline copper, some

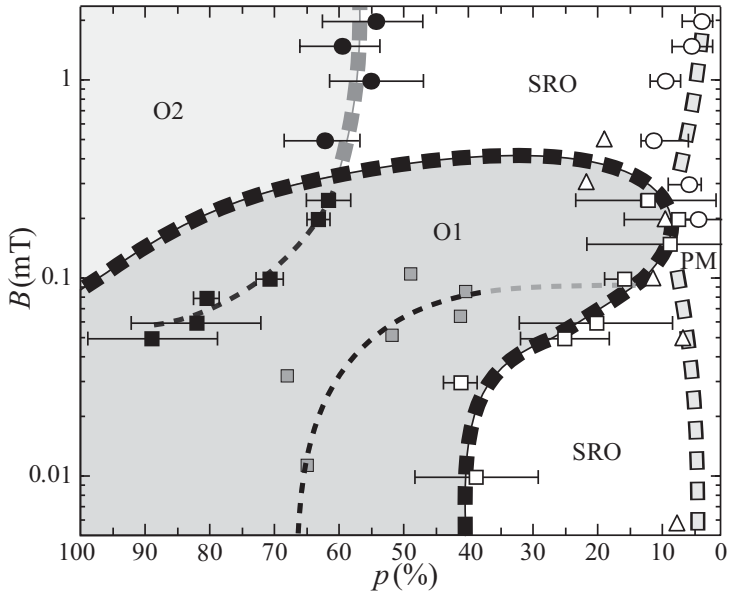

Figure 25: The suggestive phase diagram. Two ordered regions (O1 and O2) exist, together with two regions with precursory short range order (SRO). The thin dashed lines inside the O1 region indicate changes of slope of the irreversible behavior.

irreversible effects were also detected, but under different circumstances [55]: after a magnetic field sweep from 1 mT to zero and back, an increase in entropy was observed at a certain entropy range. This effect was associated with the reaching of a first order phase transition boundary and the resulting supercooling [56, 57]. The irreversibility observed in lithium is, however, of different nature: in copper, a large field sweep (from 0 to 1 mT) was needed to reveal these effects, while in lithium, the required field changes are small and continuous.

5.9 Phase diagram

Many observations presented above indicate the existence of several regions in the $p-B$ plane with different characteristics. Here, we construct a suggestive phase diagram (Fig. 25) of the lithium nuclear spin system based on the observations presented in this paper.

The different turning points of the irreversibility data are used as starting points in constructing the phase diagram: the data can be fitted piecewise linear, and there exist two or three points, depending on the field, where

the slope apparently changes. The first point is where the irreversible effects start (marked as open boxes in Fig. 25). At the second point, the slope changes to steeper at small fields (grey boxes in Fig. 25). At high fields, there exists yet another turning point; there the slope turns into negative (black boxes in Fig. 25). This point denotes the position of maximal irreversible effects at that field. The thick black dashed line in Fig. 25 encloses the the region, where we observe nonadiabatic effects. There is strong evidence for the existence of order in this region, and we call this region O1, Ordered Phase 1. At the grey boxes, there is a clear change in the irreversible behavior in the system, but the character at these points remains unclear.

In addition to the irreversible effects, we observe also other kind of deviations from a paramagnetic behavior. The low frequency anomaly in the NMR frequency spectra develops at quite low polarizations. Its development is not abrupt, but rather a gradual process, and we cannot point out any specific point to mark its onset. However, also the susceptibility deviates from a paramagnetic behavior in this region (Fig. 13); we can use this data to characterize the behavior here. We include in the phase diagram the points where the simple paramagnetic relation between susceptibility and polarization fails (section 5.5, marked with triangles in Fig. 25), We suggest, that beyond these points, a considerable amount of precursory short range order (SRO) develops, while at lower polarizations, the system is completely disordered (PM). We draw the lower dashed light grey line with black outline to denote this border line.

At higher fields, some further points are drawn in the figure: we plot the points where the entropy saturates and the heat capacity has a maximum (solid circles from Fig. 9, same symbols in Fig. 25), along which the dashed grey line is drawn. We suggest that this line denotes the onset of the high-polarization adiabatic phase, which we mark as O2. Finally, we mark the points, where the entropy parts from its high temperature expansion (open circles in Figs. 9 and 25). We draw the upper dashed light grey line with black outline on these points. We interpret the deviation from the HTE as being due to the development of considerable precursory short range order (SRO), which later develops into O2.

6 DISCUSSION AND CONCLUSIONS

We have studied for the first time the nuclear magnetic ordering in lithium. The estimate for the critical temperature is $\sim$ 350 nK at zero field. Our tentative phase diagram for the system has two separate regions with considerable short range order as precursors to two ordered phases with distinctly

different characteristics: one has a nonadiabatic character, whereas the nonadiabatic effects disappear when the second ordered region is reached. The nonadiabatic state could be explained by the existence of a domain structure: the nonadiabaticities occur when domain walls move frictionally. The domain size reaching the sample dimensions could explain the adiabatic state that is obtained at the highest polarizations. Many of the observed features fit in a ferromagnetic picture, but the present experiments can not rule out other ordered structures.

We observed nonadiabatic effects in the spin system at low fields ($B < 0.25$ mT). These effects raise a question of the validness of our temperature measurements at these fields at the highest polarizations (the higher fields are still reliable, since there is no irreversible behavior). Since we calculate the temperature from the change in susceptibility, there might be some error because some of the change is caused by these irreversible effects, and not by the heating applied on the system. The error cannot, however, be very large, because the observed changes $\Delta\chi/\chi$ are very small, except at the very highest polarizations at fields $B < 0.05$ mT.

The susceptibility at zero field forms a plateau at polarizations above $\sim 70\%$, and the absolute value of susceptibility at the plateau is very large, 11 – 12 (SI units). The Weiss temperature could not be determined unambiguously because of scatter. The inverse susceptibility (Fig. 14) appears to be slightly elevated from the Curie law, i.e. the data seems to have slightly too steep a slope. This may be accidental, but it may also result from an error in the calibration of the absolute value of susceptibility, the calibration coefficient being slightly too small. If this were true, the polarization scale would then also be by the same amount too small. The temperature scale would not, as a first approximation, be affected by this problem, since calibration against the high temperature expansion lifts its direct dependence on the absolute scale of the susceptibility. The shapes of the susceptibility curves in Figs. 11–13 would not be affected either, since both axes would be scaled. The calibration cannot, however, be very much faulted, since the highest polarization values at some of the measurements are quite close to 100%. If we were to adjust the polarization scale upwards, some points might have $p > 100\%$, which is impossible.

One can also discuss the validity of our polarization determination. We measure the susceptibility at 3 and 7 mT, and calculate the polarization using a relation that is valid in the paramagnetic state. However, we suggest a phase diagram, where the phase boundary lines seem to continue to the region of these fields, suggesting that the spin system is ordered there as well. Then the paramagnetic χ vs. p relations might not apply any more. However, if this fact gives rise to a large error in the polarization scale, it is surprising

that the initial polarizations calculated using this relation agree quite well with the expected initial polarizations calculated from the polarizing field, temperature and time.

Another aspect of our experiment was to study the electronic properties in lithium at ultralow temperatures: to search for its ambient pressure superconductivity. We cooled a bulk sample of lithium down to (105 ± 10) μK. We did not observe superconductivity, but our experiment sets a new upper limit to its occurrence, the new limit being more than an order of magnitude lower than the earlier upper limit. Since most theoretical calculations suggest superconductivity already at higher temperatures, they must have left out some important factor that suppresses its occurrence.

The constant α determining low field spin lattice relaxation (Eq. 7) is affected by magnetic impurities: Ideally, in a pure sample, it has a value 2 - 3, but in a magnetically contaminated sample, its value can be elevated. We measured a value $\alpha \sim 2.8$. This value evidences that the magnetic impurities are not important for the behavior of the nuclei. If the electronic system were much affected by these impurities, so would certainly the nuclear spins be as well. We can then conclude, that the effect of the magnetic impurities on the absence of the superconducting state is probably not very large.

Several estimates of the electron-electron and electron-phonon interactions for lithium have been made. Calculations suggest $\lambda = 0.3 - 0.4$ for the electron phonon coupling parameter [8, 58]. The conventional value for the electron electron repulsion parameter for simple metals is $\mu^* = 0.1$; using these parameters, the McMillan equation [59] gives a very high critical temperature, $T_c \sim 1$ K. Some calculations suggest a higher repulsion parameter [10, 11]; A very much larger μ^* than the simple metal value would indeed be needed to explain the upper limit for T_c reported here.

In the high pressure form, the critical temperature of lithium depends strongly on pressure. At lowest, a T_c for superconductivity has been observed at 5.47 K at a pressure of 20.3 GPa. If the T_c in the compressed state can be lowered further to the milli-Kelvin regime, studies of the interplay between superconductivity and nuclear magnetism will be interesting.

ACKNOWLEDGMENTS

This work was financially supported by the Academy of Finland (Finnish Centre of Excellence Program 2000-2005) and by the European Union (large scale facility program ULTI-III). KJ appreciates the support by Finnish National Gradute School in Materials Physics. The work by Johanna Uusvuori in designing and characterizing the magnetic shields for the superconductiv-

ity experiment is acknowledged. We thank Prof. Michael Steiner for useful discussions.

References

[1] S. Rehmann, T. Herrmannsdörfer, and F. Pobell, Phys. Rev. Lett. **78**, 1122 (1997).

[2] M. Seibold, T. Herrmannsdörfer, and F. Pobell, J. Low Temp. Phys. **110**, 363 (1998).

[3] T. Herrmannsdörfer, Physica B **280**, 368 (1998).

[4] T. Knuuttila, J. Tuoriniemi, and K. Lefmann, Phys. Rev. Lett. **85**, 2573 (2000).

[5] T. Herrmannsdörfer and Dimitrii Tayurskii, J. Low Temp. Phys. **124**, 257 (2001).

[6] P. B. Allen and M. L. Cohen, Phys. Rev. **187**, 525 (1969).

[7] D. A. Papaconstantopoulos, L. L. Boyer, B. M. Klein, A. R. Williams, V. L. Morruzzi, and J. F. Janak, Phys.Rev.B **15**, 4221 (1977).

[8] A. Y. Liu and M . L. Cohen, Phys. Rev. B **44**, 9678 (1991).

[9] A. Y. Liu and A. A. Quong, Phys. Rev. B **53**, R7575 (1996).

[10] Y. G. Jin and K. J. Chang, Phys. Rev. B **57**, 14684 (1998).

[11] C. F. Richardson and N. W. Ashcroft, Phys. Rev. B **55**, 15130 (1997).

[12] T. L. Thorp, B. B. Triplett, W. D. Brewer, M. L. Cohen, N. E. Phillips, D. A. Shirley, and J. E. Templeton, J. Low Temp. Phys. **3**, 589 (1970).

[13] K. M. Lang, Ari Mitzel, J. Mortara, E. Hudson, J. Hone, Marvin L. Cohen, A. Zettl, and J. C. Davis, J. Low Temp. Phys. **114**, 445 (1999).

[14] T. H. Lin and K. J. Dunn, Phys. Rev. B **33**, 807 (1986).

[15] K. Shimizu, H. Ishikawa, D. Takao, T. Yagi, and K. Amaya, Nature **419**, 597 (2002).

[16] V. V. Struzhkin, M. I. Eremets, W. Gan, H. Mao, and R. J. Hemley, Science **298**, 1213 (2002).

[17] S. Deemyad and J. S. Schilling, Phys. Rev. Lett. **91**, 167001 (2003).

[18] C. Reale, Phys. Lett. **55A**, 165 (1975).

[19] A. S. Oja and O. V. Lounasmaa, Rev. Mod. Phys., **69**, 1 (1997).

[20] W. Schwarz and O. Blaschko, Phys. Rev. Lett. **65**, 3144 (1990) and references therein. An illustration of the 9R lattice structure is given e.g. in A. Y. Liu and Marvin L. Cohen, Phys. Rev. B, **44**, 9678 (1191); and Y. R. Wang and A. W. Overhauser, Phys. Rev. B, **34**, 8401 (1986).

[21] A. G. Anderson, Phys. Rev. **125**, 1517 (1962).

[22] A. Abragam and M. Goldman, *Nuclear Magnetism: order and disorder*, Clarendon Press, Oxford (1982) and references threin.

[23] M. T. Huiku and M. T. Loponen, Phys. Rev. Lett. **49**, 1288 (1982).

[24] P. J. Hakonen, S. Yin, and K. K. Nummila, Europhys. Lett. **15**, 677 (1991).

[25] S. Kawarazaki, N. Kunitomi, J. R. Arthur, R. M. Moon, W. G. Stirling, ans K. A. McEwen, Phys. Rev. B **37**, 5336 (1988). K. A. McEwen and W. G. Stirling, Physica (Amsterdam) **156 − 157B**, 754 (1989).

[26] Yoshihiro Koike, Haruhiko Suzuki, and Satoshi Abe, J. Low Temp. Phys. **101**, 617 (1995).

[27] W. P. Halperin, C. N. Archie, F. B. Rasmussen, R. A. Buhrman, and R. C. Rickhardson, Phys. Rev. Lett. **32**, 927 (1974).

[28] J. P. Ekström, J. F. Jacquinot, M. T. Loponen, J. K. Soini, and P. Kumar, Physica (Amsterdam) **98B**, 45 (1979).

[29] A. S. Oja, A. J. Annila, and Y. Takano, J. Low Temp. Phys., **85**, 1 (1991).

[30] J. T. Tuoriniemi, T. A. Knuuttila, K. Lefmann, K. K. Nummila, and W. Yao, Phys. Rev. Lett. **84**, 370 (2000).

[31] R. Berliner and S. A. Werner, Phys. Rev. B **34**, 3586 (1986).

[32] P. Jauho and P. V. Pirilä, Phys. Rev. B **1**, 1 (1970).

[33] A. G. Anderson and A. G. Redfield, Phys. Rev. **116**, 583 (1959).

[34] M. Goldman, *Spin Temperature and Nuclear Magnetic Resonance in Solids*, Clarendon Press, Oxford (1970), p.51-57.

[35] W. A. Roshen and W. F. Saam, Phys. Rev. B **22**, 5495 (1980).

[36] W. A. Roshen and W. F. Saam, Phys. Rev. B **26**, 2644 (1982).

[37] Alfa Aesar, Johnson Matthey GmbH, P.O.Box 110765, D-76057 Karlsruhe, Germany.

[38] J. T. Tuoriniemi, K. I. Juntunen, and J. M. Uusvuori, Physica B **329**, 1294 (2003).

[39] W. Yao, T. A. Knuuttila, K. K. Nummila, J. E. Martikainen, A. S. Oja, and O. V. Lounasmaa, J. Low Temp. Phys. **120**, 121 (2000).

[40] T. A. Knuuttila, J. T. Tuoriniemi, K. Lefmann, K. I. Juntunen, F. B. Rasmussen, and K. K. Nummila, J. Low Temp. Phys. **123**, 65 (2001).

[41] Cryoperm 10, Vacuumschmeltze GmbH, Hanau, Germany.

[42] M. Hansen, Constitution of Binary Alloys, McGraw-Hill, New York, 1958.

[43] Ch. Buchal, F. Pobell, R. M. Mueller, M. Kubota, and J. R. Owers-Bradley, Phys. Rev. Lett. **50**, 64 (1983).

[44] A. A. Abrikosov and L. P. Gor'kov, Sov. Phys. JETP **12**, 1243 (1961).

[45] K. I. Juntunen and J. T. Tuoriniemi, to be published in J. Low Temp. Phys., (2005).

[46] F. Pobell, "*Matter and Methods at Low Temperatures*", Springer-Verlag, Berlin Heidelberg (1992).

[47] Applied Physics Systems, 1245 Space Park Way, Mountain View, CA 94043 USA.

[48] A. G. Anderson, Phys. Rev. **115**, 863 (1959).

[49] K. I. Juntunen and J. T. Tuoriniemi, to be published (2005).

[50] K. I. Juntunen and J. T. Tuoriniemi, Phys. Rev. Lett. **93**, 157201 (2004).

[51] J. T. Tuoriniemi and K. I. Juntunen, J. Low Temp. Phys., **135**, 513 (2004).

[52] P. L. Moyland, R. Kumar, J. Xu, and Y. Takano, Phys. Rev. B **48**, 14020 (1993).

[53] M. A. Ruderman and C. Kittel, Phys. Rev. **96**, 99 (1954).

[54] H. Ibach and H. Lüth, "*Solid-State Physics*", Springer-Verlag, Berlin Heidelberg (1996).

[55] M. T. Huiku, T. A. Jyrkkiö, J. M. Kyynäräinen, M. T. Loponen, O. V. Lounasmaa, and A. S. Oja, J. Low Temp. Phys. **62**, 433 (1986).

[56] M. T. Huiku, T. A. Jyrkkiö, J. M. Kyynäräinen, A. S. Oja, and O. V. Louansmaa, Phys. Rev. Lett. **53**, 1691 (1984).

[57] A. J. Annila, Physica B **165** –**166**, 783 (1990).

[58] Amy Y. Liu, Andrew A. Quong, J. K. Freericks, E. J. Nicol, and Emily C. Jones, Phys. Rev. B **59**, 4028 (1999).

[59] W. L. McMillan, Phys. Rev. **167**, 167 (1968).